

RESEARCH ARTICLE

G-CSF Receptor Deletion Amplifies Cortical Bone Dysfunction in Mice With STAT3 Hyperactivation in Osteocytes

Tsuyoshi Isojima,^{1,2} Emma C Walker,¹ Ingrid J Poulton,¹ Narelle E McGregor,¹ Ian P Wicks,³ Jonathan H Gooi,^{1,4} T John Martin,^{1,5} and Natalie A Sims^{1,5}

¹St. Vincent's Institute of Medical Research, Fitzroy, Australia

²Department of Pediatrics, Teikyo University School of Medicine, Tokyo, Japan

³Walter and Eliza Hall Institute, Parkville, Australia

⁴Bio21 Molecular Science and Biotechnology Institute, Parkville, Australia

⁵The University of Melbourne, Department of Medicine at St. Vincent's Hospital, Fitzroy, Australia

ABSTRACT

Bone strength is determined by the structure and composition of its thickened outer shell (cortical bone), yet the mechanisms controlling cortical consolidation are poorly understood. Cortical bone maturation depends on SOCS3-mediated suppression of IL-6 cytokine-induced STAT3 phosphorylation in osteocytes, the cellular network embedded in bone matrix. Because SOCS3 also suppresses granulocyte-colony-stimulating factor receptor (G-CSFR) signaling, we here tested whether global G-CSFR (*Csf3r*) ablation altered bone structure in male and female mice lacking SOCS3 in osteocytes, (*Dmp1^{Cre}:Socs3^{ff}* mice). *Dmp1^{Cre}:Socs3^{ff}:Csf3r^{-/-}* mice were generated by crossing *Dmp1^{Cre}:Socs3^{ff}* mice with *Csf3r^{-/-}* mice. Although G-CSFR is not expressed in osteocytes, *Csf3r* deletion further delayed cortical consolidation in *Dmp1^{Cre}:Socs3^{ff}* mice. Micro-CT images revealed extensive, highly porous low-density bone, with little true cortex in the diaphysis, even at 26 weeks of age; including more low-density bone and less high-density bone in *Dmp1^{Cre}:Socs3^{ff}:Csf3r^{-/-}* mice than controls. By histology, the area where cortical bone would normally be found contained immature compressed trabecular bone in *Dmp1^{Cre}:Socs3^{ff}:Csf3r^{-/-}* mice and greater than normal levels of intracortical osteoclasts, extensive new woven bone formation, and the presence of more intracortical blood vessels than the already high levels observed in *Dmp1^{Cre}:Socs3^{ff}* controls. qRT-PCR of cortical bone from *Dmp1^{Cre}:Socs3^{ff}:Csf3r^{-/-}* mice also showed more than a doubling of mRNA levels for osteoclasts, osteoblasts, RANKL, and angiogenesis markers. The further delay in cortical bone maturation was associated with significantly more phospho-STAT1 and phospho-STAT3-positive osteocytes, and a threefold increase in STAT1 and STAT3 target gene mRNA levels, suggesting G-CSFR deletion further increases STAT signaling beyond that of *Dmp1^{Cre}:Socs3^{ff}* bone. G-CSFR deficiency therefore promotes STAT1/3 signaling in osteocytes, and when SOCS3 negative feedback is absent, elevated local angiogenesis, bone resorption, and bone formation delays cortical bone consolidation. This points to a critical role of G-CSF in replacing condensed trabecular bone with lamellar bone during cortical bone formation. © 2022 American Society for Bone and Mineral Research (ASBMR).

KEY WORDS: CORTICAL BONE; OSTEOCYTE; VASCULARIZATION; JAK/STAT

Introduction

Cortical structure is a crucial determinant of bone strength. Cortical bone arises during embryonic osteogenesis initially as the diaphyseal bone collar and continues to form during growth by coalescence and compaction of trabecular bone arising from the growth plate, with entrapment of blood vessels.^(1,2) This compact, disordered bone is gradually replaced with a stronger lamellar bone structure through endosteal remodeling and deposition of new bone by modeling on the periosteal

surface.^(3,4) Cortical bone formation therefore includes consolidation of structural elements resulting from pore closure, a transition from less organized and less mineralized bone to mature lamellar structure, and an accumulation of high-density bone.^(1,4)

The underlying mechanisms controlling cortical bone maturation remain poorly understood. We previously reported delayed cortical bone consolidation in mice with a prolonged and amplified Signal Transducer and Activator of Transcription 3 (STAT3) phosphorylation response in osteocytes.⁽⁵⁾ In these mice (*Dmp1^{Cre}:Socs3^{ff}* mice), STAT3 phosphorylation was amplified by targeted

Received in original form January 4, 2022; revised form June 27, 2022; accepted July 16, 2022.

Address correspondence to: Natalie A Sims, St. Vincent's Institute of Medical Research, 9 Princes Street, Fitzroy, VIC 3065, Australia. E-mail: nsims@svi.edu.au
Additional Supporting Information may be found in the online version of this article.

Journal of Bone and Mineral Research, Vol. 00, No. 00, Month 2022, pp 1–15.

DOI: 10.1002/jbmr.4654

© 2022 American Society for Bone and Mineral Research (ASBMR).

genetic deletion of the intracellular STAT3 signaling inhibitor SOCS3 (Suppressor of Cytokine Signaling 3) in *Dmp1^{Cre}*-expressing cells (including osteocytes and late osteoblasts). This hyperactivation of STAT3 led to continued formation of osteoclasts within the developing cortical bone, which prevented its consolidation.⁽⁵⁾ When these mice were exercised on a treadmill, cortical consolidation was delayed still further.⁽⁶⁾ A similar phenotype of delayed cortical bone formation was also observed in a second model when SOCS3 was deleted earlier in the osteo-chondral lineage using *Col2-Cre*.⁽⁷⁾ This indicated that STAT3-activating cytokines requiring SOCS3 for intracellular negative feedback must be suppressed for normal cortical bone formation.

STAT3 is a ubiquitous intracellular signaling molecule phosphorylated by multiple JAK/STAT cytokine receptors,⁽⁸⁾ and SOCS3 provides negative feedback for their STAT3-phosphorylation.⁽⁹⁾ One of these receptors is gp130 (glycoprotein 130), the common signal transducer used by the IL-6 family of cytokines. By targeted deletion of gp130 in *Dmp1^{Cre}:Socs3^{fl/fl}* mice, we showed that this family of cytokines is responsible, at least in part, for the cortical bone phenotype and the high level of STAT3 phosphorylation in *Dmp1^{Cre}:Socs3^{fl/fl}* osteocytes.⁽¹⁰⁾ However, IL-6 itself was not the major contributor,⁽⁵⁾ suggesting other members of the gp130-signaling cytokine family, such as IL-11, leukemia inhibitory factor (LIF), oncostatin M (OSM), and cardiotrophin, are involved, also since they all stimulate both bone formation and resorption.⁽¹¹⁻¹⁶⁾

We needed to consider that SOCS3 also inhibits STAT3 phosphorylation downstream of the granulocyte-colony-stimulating factor receptor (G-CSFR).⁽⁹⁾ In our previous work, when we crossed the *Dmp1^{Cre}:Socs3^{fl/fl}* mice with a gp130 (*Il6st*)-deficient mouse to resolve the phenotype,⁽¹⁰⁾ we also set up experiments to cross *Dmp1^{Cre}:Socs3^{fl/fl}* mice with *Csf3r* null mice on the assumption that no effect would be observed, given the lack of G-CSFR in osteoblasts and osteocytes.^(17,18) To our surprise, the phenotype became more marked. In the present work, we define the unexpected phenotype found and identify possible causes.

Although there is no clear physiological role of G-CSF in regulating bone structure, it has pharmacological effects on the skeleton in vivo. Administration of G-CSF to mobilize hemopoietic stem and progenitor cells from marrow to the circulation depletes bone surface osteoblasts within days,⁽¹⁷⁾ resulting in suppressed bone formation on both endocortical and trabecular surfaces.^(19,20) G-CSF administration also reduces mRNA levels of osteocyte markers and changes osteocyte morphology.⁽²¹⁾ G-CSF administration also stimulates osteoclast formation.⁽²²⁾ The mechanisms by which pharmacological G-CSF acts on the osteoblast lineage or on osteoclasts have not been fully resolved, although there is evidence for at least two pathways: (1) loss of supporting signals from resident macrophages within the bone marrow,⁽¹⁹⁾ and (2) suppression of bone formation via the sympathetic (adrenergic) nervous system.^(18,21) What is clear is that pharmacological effects of G-CSF on the skeleton result from indirect action on the osteoblast lineage, since G-CSF receptor is not expressed by osteoblasts or osteocytes.^(17,18)

We show here that, although G-CSFR null mice have no basal phenotype, G-CSFR deletion in the absence of SOCS3 in osteocytes exaggerates the profound defect in cortical bone consolidation caused by osteocyte deletion of SOCS3. This is characterized by a very high level of cortical resorption and vascularization, and associated with excessive STAT3 and STAT1 phosphorylation in osteocytes. This points to a new influence of G-CSF in bone as a physiological suppressor of bone

formation, bone resorption, and bone vascularization, and as a stimulus of cortical bone consolidation.

Materials and Methods

Mice

Dmp1^{Cre}:Socs3^{fl/fl} mice were generated as previously described⁽⁵⁾ by crossing *Dmp1-Cre* (*Tg(Dmp1-cre)*^{1^{qfe}}) mice (containing the *Dmp1* 10-kb promoter region) provided by Lynda Bonewald (University of Kansas, Kansas City, MO, USA),⁽²³⁾ with *Socs3* floxed (*Socs3^{tm1^{Wsa}}*) mice, provided by Warren Alexander (Walter and Eliza Hall Institute of Medical Research, Melbourne, Australia).⁽²⁴⁾ *Csf3r* null mice⁽¹⁹⁾ were obtained from Ian Wicks (Walter and Eliza Hall Institute of Medical Research). All had been previously backcrossed to a C57BL/6 background. To compare *Dmp1^{Cre}:Socs3^{fl/fl}:Csf3r^{-/-}* and *Dmp1^{Cre}:Socs3^{fl/fl}* mice, littermate controls were obtained by crossing *Dmp1^{Cre}:Socs3^{fl/fl}* mice with *Csf3r^{-/-}* mice, then breeding from *Dmp1^{Cre}:Socs3^{fl/fl} Csf3r^{+/-}* pairs. Samples collected to assess the basal phenotype of *Csf3r^{-/-}* mice compared with their own littermate wild-type controls were obtained directly from the colony of Ian Wicks (Walter and Eliza Hall Institute of Medical Research).

Bone samples were collected at 6, 12, 16, or 26 weeks of age (as indicated in figure legends) after injection with calcein (20 mg/kg) at 3 and 10 days before collection.⁽¹¹⁾ When samples from 12-week-old mice were collected, one femur was flushed of marrow and the bone shaft was collected for extracting RNA.⁽²⁵⁾ Sample size ($n = 10$) was based on previous studies using micro-CT and histomorphometry. No explicit power analysis was performed. All were fasted overnight before tissue collection. All analyses below were conducted with the observer being blinded to the genotype of the samples. Mice were group housed and supplied with water and standard mouse cubes (1.14% calcium, 2 IU vitamin D3/kg, 20% protein: 133 Barastoc, Ridley AgriProducts, Melbourne, Australia) *ad libitum*; no fighting was observed in any of the cages. All animal procedures were conducted with approval of the St. Vincent's Health Melbourne Animal Ethics Committee.

Micro-CT

Femora of *Dmp1^{Cre}:Socs3^{fl/fl}* and *Dmp1^{Cre}:Socs3^{fl/fl}:Csf3r^{-/-}* mice were scanned using a Skyscan 1076 (6 and 12 weeks of age) or 1276 (26 weeks of age, *Csf3r^{-/-}* mice and their controls) micro-CT system (Bruker, Aartselaar, Belgium) to access their basal phenotypes as described previously^(26,27) with the following modifications. Projections were acquired over 180° (step of 0.4–0.7°) with the following settings: 44 kV and 220 mA, 9 μm voxel resolution, 0.5 mm aluminum filter, 2300 ms exposure time (481 ms for 26-week-old samples), and frame averaging = 1. Images were reconstructed and analyzed using NRecon (Bruker, versions 1.6.9.8 [6- and 12-week-old samples] or 1.7.1.0 [26-week-olds]), Dataviewer (Bruker, version 1.5.4.0), and CT Analyzer (Bruker, version 1.17.7.2+). 3D-tomographic volume images of bone were created using CTvox (Bruker, version 3.2.0). Femoral length was measured in all collected samples. For metaphyseal and diaphyseal analyses, the regions of interest were 15% of the total femur length, commencing at a distance equal to 7.5% or 30%, respectively of femur bone length from the distal femoral growth plate, as indicated in figure legends; the cortical region includes the midpoint of the diaphysis. Cortical porosity measurements were determined

using a global threshold minimum of 0.632 g/cm³ CaHA (calcium hydroxyapatite) for bone.

Because this model does not form normal trabecular or cortical bone structures, to quantify morphological and tissue mineral content changes during growth objectively, we used a new method to measure bone areas of low-, medium-, and high-density bone.^(10,28) This method uses an unbiased thresholding algorithm, which segments the pixels into different classes set based on the gray level intensities within the control image set.⁽²⁹⁾ This overcomes the requirement to subjectively segment bone into “trabecular” and “cortical” components. We therefore determined nonparametric unsupervised four-level Otsu thresholding with CT Analyzer (Bruker, version 1.17.7.2+) according to our previously published methods.^(6,10,28) The threshold ranges for the three density levels of bone measured were as follows: low density (0.661–1.0174 g/cm³ CaHA); mid-density (1.0174–1.3639 g/cm³ CaHA), and high density (>1.3639 g/cm³ CaHA). The lowest-density quartile was discarded because it contained non-bone material. Bone volumes at each of the three densities were measured and are expressed relative to the total cross-sectional volume. In addition, data were extracted for each 9 μm slice within the region of interest, and these areas at each density are reported as bone area as a percentage of total cross-sectional area for each slice, as previously described.^(6,10,28)

Histology, immunohistochemistry, histomorphometry, and flow cytometry

Left tibiae from 12-week-old mice were infiltrated and embedded in methylmethacrylate and sectioned at 5 μm thickness for histomorphometric analysis as previously described.⁽³⁰⁾ Sections were stained with Toluidine blue or Xylenol orange as previously described.⁽¹¹⁾ Right tibiae were fixed in 4% paraformaldehyde in 0.05 M phosphate buffered saline (PBS) for 24 hours, decalcified in ethylene diamine tetraacetic acid (EDTA), and embedded in paraffin.^(12,31) Four μm paraffin sections were used for Ploton silver staining and tartrate-resistant acid phosphatase (TRAP) staining, as previously described.^(12,32,33) Immunohistochemistry was also carried out for phospho-STAT1, phospho-STAT3, total STAT3, and endomucin, as previously described⁽¹²⁾ with the following modifications. Endogenous peroxidase was blocked for 20 minutes in 3% H₂O₂ in 100% methanol. Sections were permeabilized for 15 minutes in 0.5% trypsin in PBS. After rinsing with 0.05 M PBS, they were blocked with 10% swine serum in PBS with 0.01% Tween 20 (TBS) for 60 minutes or TNB (Renaissance TSA indirect [Tyramide Signal Amplification, PerkinElmer Life Sciences, Waltham, MA, USA; #NEL700]) for 30 minutes before primary antibody was applied. They were incubated with antibodies to phospho-STAT1 (Tyr701) (Cell Signaling, Danvers, MA, USA; #7649 1:50), phospho-STAT3 (Tyr705) (Cell Signaling #9131, 1:100), total STAT3 (Cell Signaling #9139, 1:50), endomucin (Invitrogen, Carlsbad, CA, USA; #14-5851-81, 1:200) or IgG control (rabbit IgG, Dako, Glostrup, Denmark) in a humidified chamber at room temperature overnight. A secondary antibody (swine anti-rabbit, Dako) was applied for 45 minutes in TBS at 1:250, followed by streptavidin horseradish peroxidase (Dako) at 1:500 in the same blocking solution (TBS) for 45 minutes, then biotin tyramine at 1:50 in amplification diluent for 7 minutes (TSA Biotin System Kit, PerkinElmer). This was followed by streptavidin horseradish peroxidase (Dako) at 1:500 in the same blocking solution (TBS) for 45 minutes. They were rinsed in TBS containing Triton 1000 between each step. Antibody binding was visualized using a diaminobenzidine

colorimetric kit (Dako), following which, sections were counterstained with Mayer's hematoxylin solution for 90 seconds, rinsed in Scott's tap water, then dehydrated with graded ethanols (70%, 90%, 100%, 100%) and mounted with DePex.

Histomorphometric measurements of phospho-STAT1, phospho-STAT3, and total STAT3-positive osteocytes, osteoclast surface and numbers, vessel areas and numbers, and pore areas were all carried out in cortical bone of the lateral tibial metaphysis, commencing 1110 μm below the distal end of the lateral growth plate and extending for 1480 μm (8 fields at 40× magnification), using the OsteoMeasure system (Osteometrics Inc., Decatur, GA, USA). This equates to a region approximately 10% of the length of the bone, commencing at a distance below the growth plate equal to approximately 7.5% of the length of the bone. To measure the region of cortex actively undergoing consolidation, the lateral side of the tibia was chosen because immature cortical bone is readily detected in this region; we measured a 100-μm-wide region of interest commencing 50 μm from the periosteal edge. All histomorphometric measurements were conducted with the observer being blinded. Images of the bone were captured using a Leica (Buffalo Grove, IL, USA) DM2000 microscope with an Olympus (Tokyo, Japan) DP72 microscope camera, connected to a computer.

For flow cytometry, bone marrow from femurs and tibiae of 12 week old mice were collected into cold 2% fetal bovine serum in PBS, stained on ice for 30 minutes with antibodies to CD11b APC/Cy7 and Gr-1 FITC (both BioLegend, San Diego, CA, USA), and washed in PBS. Cell populations were assessed on an LSR Fortessa flow cytometer (BD Biosciences, Macquarie Park, Australia). Flow cytometric analysis was performed on FlowJo v10 (Ashland, OR, USA) with dead cells and doublets excluded. Neutrophils were defined by Gr1⁺/CD11b⁺ expression.

Three-point bending test

Mechanical properties of femora were derived from three-point bending tests using a Bose ElectroForce Biodynamic 5500 Test Instrument (Eden Prairie, MN, USA), as described previously.⁽³⁴⁾ Once whole-bone properties were determined, tissue-level mechanical properties were calculated using micro-CT derived data from the midshaft.⁽³⁵⁾

Real-time quantitative PCR (RT-qPCR)

RNA was isolated from homogenized marrow flushed-out femora from 12-week-old mice as previously described.⁽³⁶⁾ Briefly, flushed femora were homogenized with a LS-10-35 Polytron homogenizer in Qiazol for 4 × 5-second bursts. Extracted RNA was treated with DNase (Ambion TURBO DNA-Free Kit; Ambion Inc., Waltham, MA, USA) and measured on a NanoDrop ND1000 Spectrophotometer (Thermo Fisher Scientific, Wilmington, DE, USA), then stored at –80°C. cDNA was generated using a Tetro cDNA synthesis kit (Bioline, Meridian, Memphis, TN; #BIO-65043) according to the manufacturer's instruction. RT-qPCR was performed on a Stratagene Mx3000P QPCR system (Agilent Technologies, Santa Clara, CA, USA) with two-step cycling conditions (95°C for 10 minutes followed by 95°C for 30 seconds and 60°C for 1 minute) for 40 cycles followed by a dissociation step (95°C for 1 minute, 55°C for 30 seconds, and 95°C for 30 seconds) using Sybr Select (Thermo Fisher Scientific #4472908) as previously described.⁽³⁷⁾ Primers for *Bglap1* (osteocalcin, bone gamma-carboxyglutamate protein),⁽³⁸⁾ *Alpl* (alkaline phosphatase),⁽³⁹⁾ *Col1a1* (collagen type I alpha 1),⁽³⁹⁾ *Dcstamp*

(dendritic cell-specific transmembrane protein),⁽³⁹⁾ *Acp5* (tartrate-resistant acid phosphatase type 5)⁽⁷³⁾, *Tnfrsf11* (tumor necrosis factor ligand superfamily member 11),⁽⁴⁰⁾ *Tnfrsf11b* (tumor necrosis factor receptor superfamily member 11b),⁽⁴¹⁾ *Socs1* (suppressor of cytokine signaling 1),⁽²⁵⁾ *Bcl3* (B-cell lymphoma 3 protein homolog),⁽²⁵⁾ *Vegfa* (vascular endothelial growth factor A),⁽¹²⁾ *Hprt1* (hypoxanthine-guanine phosphoribosyltransferase 1),⁽⁴²⁾ *B2m* (beta-2 microglobulin)⁽⁴³⁾ were described previously. Primers for *Emcn* (Endomucin) (forward 5'-AGTGAGGACGGCAAAGAT-3', reverse 5'-GGGACCTT-CAGTTGTTGTTTC-3') and *Tie-1* (tyrosine-protein kinase with immunoglobulin-like and EGF-like domains 1) (forward 5'-GATTTGGTAGGCGTCTTCTC-3', reverse 5'-CTTGCCAGTCTAGGG-TATTG-3') were designed using PrimerQuest. Post-run samples were analyzed using Stratagene software MxPro and data were normalized to geometric mean of two housekeeping genes (ie, *Hprt1* and *B2m*). Relative expression was quantified using the comparative threshold cycle (Ct) method ($2^{-\text{(Gene Ct - Normalizer Ct)}}$).

Statistical analysis

In most instances, two-way ANOVA with mixed-effects analysis was used, with repeated measures for slice-by-slice comparisons because these data are from multiple measurements on the same dependent variable taken of the same samples. Sidak or Tukey post hoc tests were used to identify significant differences, as indicated in figure legends. Student's *t* test was used where only one comparison was being made. No outliers were excluded from any analyses. A $p < 0.05$ was considered significant. All statistical analyses were performed by GraphPad (La Jolla, CA, USA) Prism 9. The p values for all ANOVAs are reported in Supplemental Fig. S5.

Results

Dmp1^{Cre}:Socs3^{ff}.Csf3r^{-/-} mice show more severely disrupted skeletal structure than *Dmp1^{Cre}:Socs3^{ff}* mice

Micro-CT analysis of femora detected no significant differences in cortical bone mass or trabecular structure in 16-week-old male or female *Csf3r^{-/-}* mice compared with age- and sex wild-type controls (Supplemental Fig. S5A–F).

Since our earlier work showed bone corticalization was delayed in male and female *Dmp1^{Cre}:Socs3^{ff}* mice at 12 weeks of age and gradually recovered by 26 weeks of age,⁽⁵⁾ we evaluated cortical maturation of *Dmp1^{Cre}:Socs3^{ff}* and *Dmp1^{Cre}:Socs3^{ff}.Csf3r^{-/-}* mice at 6, 12, and 26 weeks of age. In initial raw images of femoral scans, both male and female *Dmp1^{Cre}:Socs3^{ff}* mice showed the same phenotype we observed previously at these ages⁽⁵⁾: high bone mass in the metaphysis at 6 weeks of age and porous cortical bone at 6, 12, and 26 weeks of age (males in Fig. 1A; females in Fig. 1B). When G-CSFR was deleted (in male and female *Dmp1^{Cre}:Socs3^{ff}.Csf3r^{-/-}* mice), their femoral morphology was similar to *Dmp1^{Cre}:Socs3^{ff}* at 6 weeks of age, but at 12 weeks of age they had much more metaphyseal trabecular bone than *Dmp1^{Cre}:Socs3^{ff}* mice and contained only a small amount of high-density consolidated cortical bone, and this was further from the growth plate than in *Dmp1^{Cre}:Socs3^{ff}* mice, suggesting a greater delay in cortical bone consolidation (Fig. 1A, B). This exaggeration was more substantial in male femora collected at 26 weeks of age (Fig. 1A). Female *Dmp1^{Cre}:Socs3^{ff}.Csf3r^{-/-}* mice had a survival defect of unknown cause

(Supplemental Fig. S1G, H); this precluded analysis of female *Dmp1^{Cre}:Socs3^{ff}.Csf3r^{-/-}* mice at 26 weeks of age.

To quantify the bone phenotype in *Dmp1^{Cre}:Socs3^{ff}.Csf3r^{-/-}* femora, standard manual or algorithm-based methods to distinguish trabecular and cortical bone mass^(44,45) were not suitable because the distinction between cortical and trabecular bone was often ambiguous. Therefore, we used our newly developed unbiased multiple-threshold micro-CT method, which objectively measures bone at high-, mid-, and low-density thresholds, without subjectively designating bone as trabecular or cortical.^(10,28) In male and female mice at 6 weeks of age, both *Dmp1^{Cre}:Socs3^{ff}* and *Dmp1^{Cre}:Socs3^{ff}.Csf3r^{-/-}* mice had the same amount of total metaphyseal bone, which comprised mainly low-density bone (Fig. 1C), consistent with our previous observations in *Dmp1^{Cre}:Socs3^{ff}* mice.⁽¹⁰⁾ In both male and female *Dmp1^{Cre}:Socs3^{ff}.Csf3r^{-/-}* mice, a significantly higher proportion of the metaphyseal bone was low density compared with *Dmp1^{Cre}:Socs3^{ff}* mice (male 10.2% greater, $p < 0.0001$; female 5.8% greater, $p = 0.035$). With skeletal maturation between 6 and 12 weeks of age in male and female *Dmp1^{Cre}:Socs3^{ff}* femoral metaphyses, total bone volume did not change as a proportion of metaphyseal volume, but the proportion of low-density bone decreased and the proportion of high-density bone increased, consistent with our reports of gradual, albeit delayed, maturation of *Dmp1^{Cre}:Socs3^{ff}* cortical bone.^(5,6) When G-CSFR was deleted, the proportion of low-density bone remained higher in male *Dmp1^{Cre}:Socs3^{ff}* femora at all ages (by two-way ANOVA, genotype p value < 0.0001 ; age p value < 0.0001 ; interaction p value = 0.2399) (Fig. 1C). Furthermore, unlike male *Dmp1^{Cre}:Socs3^{ff}* femora, male *Dmp1^{Cre}:Socs3^{ff}.Csf3r^{-/-}* femora showed no increase in the proportion of high-density bone with age (by two-way ANOVA, genotype p value < 0.0001 ; age p value < 0.0001 ; interaction p value < 0.0001). In female mice between 6 and 12 weeks of age, both *Dmp1^{Cre}:Socs3^{ff}* and *Dmp1^{Cre}:Socs3^{ff}.Csf3r^{-/-}* femora showed a significant reduction in the proportion of low-density bone (by two-way ANOVA, genotype p value < 0.0164 ; age p value < 0.0001 ; interaction p value = 0.2848), but only *Dmp1^{Cre}:Socs3^{ff}* femora accrued high-density bone (by two-way ANOVA, genotype p value < 0.0001 ; age p value < 0.0001 ; interaction p value < 0.0001), and total bone volume was significantly reduced at 12 weeks of age (Fig. 1C). This lack of transition from low- to high-density bone indicates a further delay in cortical bone development in both male and female *Dmp1^{Cre}:Socs3^{ff}.Csf3r^{-/-}* femora compared with the already significant delay previously described in male and female *Dmp1^{Cre}:Socs3^{ff}* mice.

Differences in femur length and shape were minor between these two mouse lines at 12 weeks of age. Femurs from female *Dmp1^{Cre}:Socs3^{ff}.Csf3r^{-/-}* mice were $< 5\%$ shorter than *Dmp1^{Cre}:Socs3^{ff}* mice, and periosteal circumference of male *Dmp1^{Cre}:Socs3^{ff}.Csf3r^{-/-}* femurs was greater by around 10% (Table 1).

Because we previously observed greater cortical resorption in the skulls of *Dmp1^{Cre}:Socs3^{ff}* mice,⁽¹⁰⁾ we also assessed calvariae of 12-week-old male and female *Dmp1^{Cre}:Socs3^{ff}.Csf3r^{-/-}* mice and observed high cortical porosity at this location also (Fig. 1D).

As the *Dmp1^{Cre}:Socs3^{ff}.Csf3r^{-/-}* femora showed a further delay in cortical bone development compared with *Dmp1^{Cre}:Socs3^{ff}* femora, and since there is a gradient of bone maturation with increasing distance from the growth plate,⁽²⁾ we assessed this by analyzing the change in proportions of low-, mid- and high-density bone in 9 μm slices from the distal to the proximal end of the femoral metaphysis, using our previously published methods.^(6,10,28) At 6 weeks of age, male and female *Dmp1^{Cre}:*

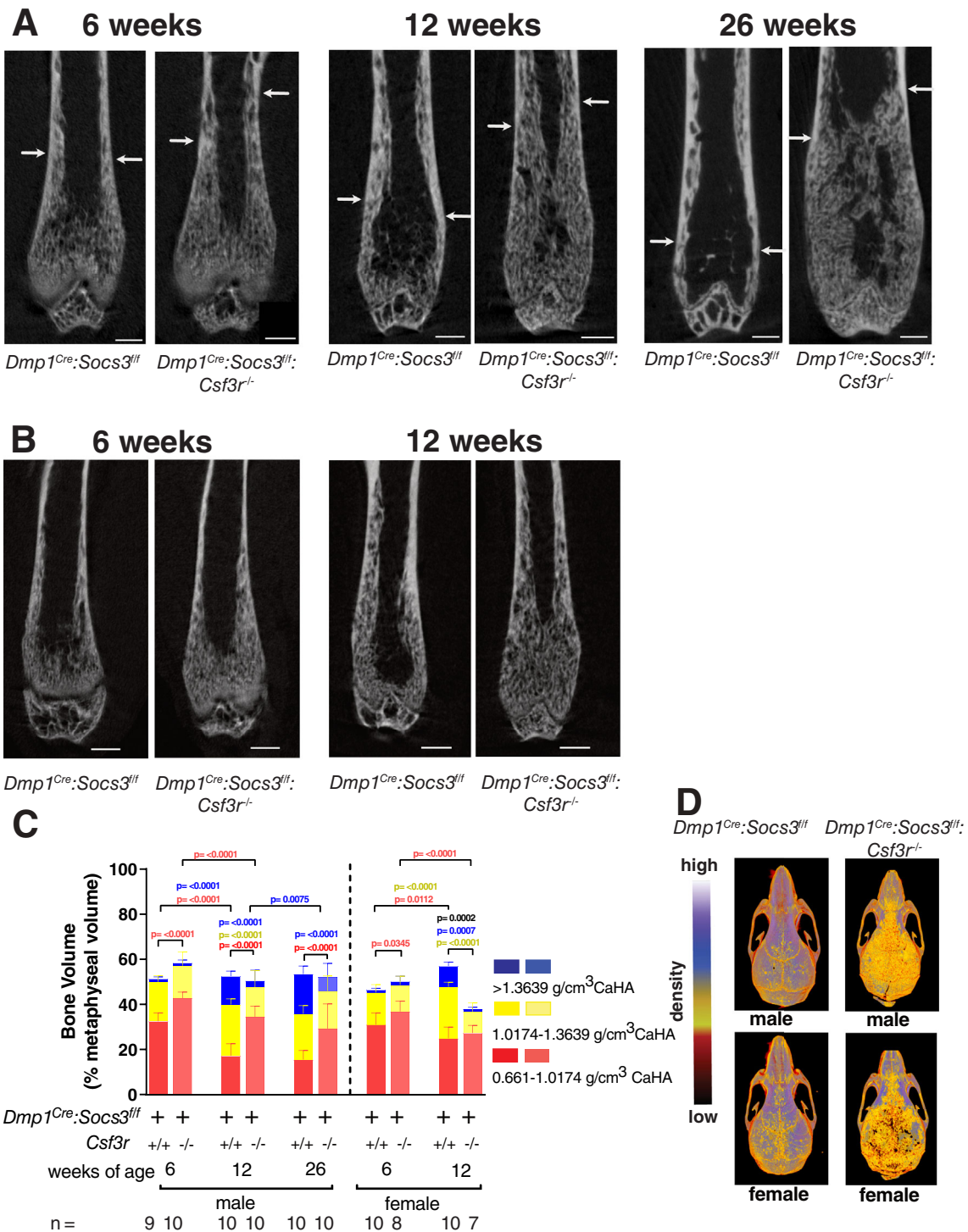


Fig. 1. The distinctive bone structure of *Dmp1^{Cre}:Socs3^{ff}:Csf3r^{-/-}* mice at 6, 12 and 26 weeks of age detected by micro-CT analyses of the metaphysis. (A, B) Representative raw micro-CT images showing a single femoral coronal slice at 6, 12, and 26 weeks of age in male (A) and female (B) *Dmp1^{Cre}:Socs3^{ff}* (left) and *Dmp1^{Cre}:Socs3^{ff}:Csf3r^{-/-}* (right) mice; scale bar = 500 μ m; arrows indicate the proximal-most point at which cortical bone was high density and consolidated, albeit porous. (C) Bone volume as a percentage of total metaphyseal volume measured at low-, mid- and high-density thresholds at 6, 12, and 26 weeks in male and female *Dmp1^{Cre}:Socs3^{ff}* (left) and *Dmp1^{Cre}:Socs3^{ff}:Csf3r^{-/-}* (right) mice. Sidak post hoc test, *n* shown at bottom of graph; colors used for *p* values match the density level of bone analyzed; data are median + interquartile range). (D) Representative images of skulls from 12-week-old male and female *Dmp1^{Cre}:Socs3^{ff}* and *Dmp1^{Cre}:Socs3^{ff}:Csf3r^{-/-}* mice. Scale on left indicates raw tissue density.

Table 1. Femoral Dimensions, Serum Biochemistry, and Three-Point-Bending Test Results From 12-Week-Old *Dmp1^{Cre}:Socs3^{ff}* and *Dmp1^{Cre}:Socs3^{ff}:Csf3r^{-/-}* Mice

Parameter	Male		Female	
	<i>Dmp1^{Cre}:Socs3^{ff}</i>	<i>Dmp1^{Cre}:Socs3^{ff}:Csf3r^{-/-}</i>	<i>Dmp1^{Cre}:Socs3^{ff}</i>	<i>Dmp1^{Cre}:Socs3^{ff}:Csf3r^{-/-}</i>
No. of samples	10	9	10	7
Femur length (mm)	13.76 ± 0.08	13.69 ± 0.12	13.56 ± 0.11	13.17 ± 0.08*
Periosteal circumference (mm)	4.89 ± 0.41	5.41 ± 0.46**	4.58 ± 0.24	4.78 ± 0.27
Craniocaudal width (mm)	1.24 ± 0.030	1.33 ± 0.044	1.17 ± 0.020	1.17 ± 0.034
Mediolateral width (mm)	1.70 ± 0.044	1.92 ± 0.050***	1.62 ± 0.033	1.69 ± 0.035
Cortical thickness (mm)	0.27 ± 0.016	0.46 ± 0.027***	0.24 ± 0.013	0.37 ± 0.031**
Serum calcium (mmol/L)	2.40 ± 0.05	2.52 ± 0.10	2.30 ± 0.05	2.30 ± 0.10
Serum phosphate (mmol/L)	1.25 ± 0.07	1.33 ± 0.05	1.19 ± 0.06	1.25 ± 0.09
Ultimate deformation (mm)	0.442 ± 0.036	0.391 ± 0.034	0.405 ± 0.021	0.329 ± 0.027
Yield force (N)	14.03 ± 0.95	15.03 ± 1.67	11.34 ± 0.63	9.25 ± 0.44
Yield deformation (mm)	0.358 ± 0.037	0.324 ± 0.032	0.263 ± 0.023	0.250 ± 0.012
Post-yield deformation (mm)	0.128 ± 0.023	0.081 ± 0.017	0.185 ± 0.027	0.124 ± 0.021
Energy to failure (mJ)	4.12 ± 0.32	3.75 ± 0.62	3.70 ± 0.39	2.43 ± 0.23
Stiffness (N/mm)	53.3 ± 18.9	53.2 ± 17.5	54.2 ± 13.4	43.1 ± 3.2
Ultimate stress (MPa)	34.25 ± 2.69	20.35 ± 1.92***	37.83 ± 2.53	26.99 ± 3.30**
Ultimate strain (%)	0.092 ± 0.008	0.087 ± 0.010	0.079 ± 0.004	0.064 ± 0.006
Yield stress (MPa)	30.87 ± 2.24	18.62 ± 1.72***	32.91 ± 2.08	22.19 ± 2.37**
Yield strain (%)	0.074 ± 0.008	0.072 ± 0.008	0.051 ± 0.005	0.049 ± 0.003
Post-yield strain (%)	0.026 ± 0.004	0.018 ± 0.004	0.037 ± 0.006	0.024 ± 0.004

Values are mean ± SD.

p* < 0.05; *p* < 0.01; ****p* < 0.0001 versus age- and sex-matched *Dmp1^{Cre}:Socs3^{ff}*.

Socs3^{ff} mice exhibited a gradual reduction in the proportion of low-density bone and an increase in the proportion of mid-density bone in the metaphysis with increasing distance from the growth plate (Fig. 2A; Supplemental Fig. 2A), indicating a gradient of bone maturation with increasing bone age. In contrast, neither male nor female 6-week-old *Dmp1^{Cre}:Socs3^{ff}:Csf3r^{-/-}* mice exhibited a reduction in the proportion of low-density bone along the metaphysis (Fig. 2B; Supplemental Fig. 2B). As previously described, 12-week-old male and female *Dmp1^{Cre}:Socs3^{ff}* mice^(6,10) showed a significant reduction in the proportion of low-density bone along the metaphysis and a gradual increase in high-density bone with increasing distance from the growth plate, indicating further maturation (males in Fig. 2C; females in Supplemental Fig. S2B). This was also observed in *Dmp1^{Cre}:Socs3^{ff}* mice at 26 weeks of age. In contrast, 12-week-old male and female *Dmp1^{Cre}:Socs3^{ff}:Csf3r^{-/-}* mice showed no significant change in the proportion of high- or low-density bone along the metaphysis at these time points (Fig. 2D, F; Supplemental Fig. S2D) indicating that the normal gradient of bone maturation was lost in these mice. Direct comparisons between *Dmp1^{Cre}:Socs3^{ff}* and *Dmp1^{Cre}:Socs3^{ff}:Csf3r^{-/-}* femora from male mice are shown at each age in Supplemental Fig. S53. From these results, cortical maturation in *Dmp1^{Cre}:Socs3^{ff}:Csf3r^{-/-}* bone was much further delayed than *Dmp1^{Cre}:Socs3^{ff}* bone. Because we did not detect a striking sex difference in *Dmp1^{Cre}:Socs3^{ff}:Csf3r^{-/-}* bone in these analyses, we focused on the males for further detailed analyses.

Dmp1^{Cre}:Socs3^{ff}:Csf3r^{-/-} bones show a further delay in cortical maturation

Since *Dmp1^{Cre}:Socs3^{ff}* bone exhibited reduced bone strength,⁽¹⁰⁾ we next tested whether the further delay in cortical maturation in *Dmp1^{Cre}:Socs3^{ff}:Csf3r^{-/-}* femora increased bone fragility. However, three-point bending tests revealed no further impairment

in strength between the two mice lines; ultimate force reached before breaking was unchanged (Fig. 3A), and stiffness and deformation were also unchanged (Table 1). Consistent with their greater “cortical” thickness (which included porous bone) (Table 1), significantly lower ultimate stress and yield stress were observed in *Dmp1^{Cre}:Socs3^{ff}:Csf3r^{-/-}* femora compared with *Dmp1^{Cre}:Socs3^{ff}* (Table 1), but this parameter assumes normal material quality and distribution of load across a nonporous cortical structure, which is clearly not the case in these samples.

Since three-point bending tests evaluate bone strength at the diaphysis, we determined whether immature cortex was also present there. Indeed, cortical porosity of *Dmp1^{Cre}:Socs3^{ff}:Csf3r^{-/-}* bone was approximately sevenfold greater than *Dmp1^{Cre}:Socs3^{ff}* bone (Fig. 3B), but total bone volume including at all density levels was not different (Fig. 3C), indicating dispersed distribution of the bone material in *Dmp1^{Cre}:Socs3^{ff}:Csf3r^{-/-}* bone. The *Dmp1^{Cre}:Socs3^{ff}:Csf3r^{-/-}* diaphysis, like the metaphysis (Fig. 1B), also had a higher proportion of low-density bone and a lower proportion of high-density bone than the *Dmp1^{Cre}:Socs3^{ff}* diaphysis (Fig. 3C).

To better understand why the bone was of low density and porous, Ploton silver staining was performed to assess the orientation of the osteocyte network in cortical bone and the presence of three of the four stages of cortical bone maturation described by Enlow in 1962: calcified cartilage, woven bone, compact whorls, and mature lamellar bone.⁽¹⁾ This revealed a unique structure within the lateral cortex of *Dmp1^{Cre}:Socs3^{ff}:Csf3r^{-/-}* tibias. Their cortical bone contained mostly compact whorls, with lamellar bone being found on the endocortical surface but separated from the compact whorl region by a channel of highly porous non-lamellar bone containing blood vessels and marrow (Fig. 3D). This “double shell” of cortical bone suggests an interruption in the normal process of cortical maturation by intracortical vascularization and resorption in *Dmp1^{Cre}:Socs3^{ff}:Csf3r^{-/-}* bone.

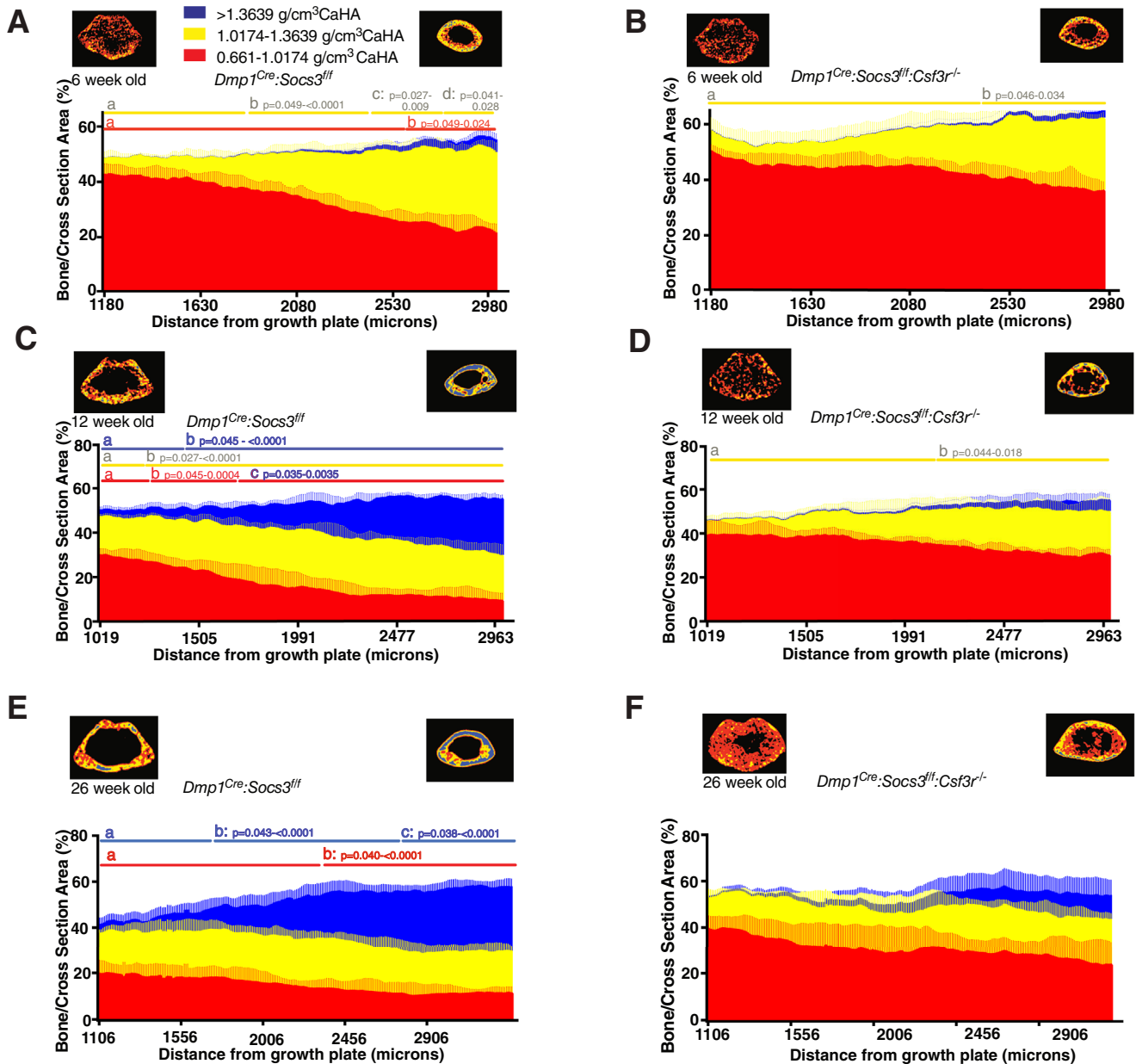


Fig. 2. A further delay in accrual of high-density bone in *Dmp1^{Cre}:Sox3^{fl/fl}:Csf3r^{-/-}* femora. Data shown is bone area as a proportion of cross-sectional area measured at low- (red), mid- (blue), and high- (yellow) density mineral thresholds from the distal to proximal end of the femoral metaphysis region at 6 (A, B), 12 (C, D), and 26 (E, F) weeks of age in male *Dmp1^{Cre}:Sox3^{fl/fl}* (A, C, E) and *Dmp1^{Cre}:Sox3^{fl/fl}:Csf3r^{-/-}* (B, D, F) mice. Values are median + interquartile range, *n* is shown in Fig. 1C. Horizontal lines with letters (eg, a, b, c, d) indicate regions that are significantly different from each other (*p* < 0.05 compared with the first measurement in the previous group (the range of *p* values < 0.05 from that point until the end of the measurement region are shown). Statistical analysis was repeated measures two-way ANOVA for each age group (density versus distance) with Tukey post hoc test and correction for repeated measures; colors correspond to the density level measured. Where no horizontal bar is shown, this means there was no statistically significant difference in that measure along the length of the bone. Pseudo-colored images based on the thresholds show a representative sample for the top and bottom slice for each group.

The *Dmp1^{Cre}:Sox3^{fl/fl}:Csf3r^{-/-}* mice exhibit increased intracortical bone resorption and formation

Since the *Dmp1^{Cre}:Sox3^{fl/fl}* phenotype was caused, at least in part, by gp130-dependent osteoclast formation within the cortical bone,⁽¹⁰⁾ we next determined whether the greater porosity in *Dmp1^{Cre}:Sox3^{fl/fl}:Csf3r^{-/-}* bone was caused by a further increase in

osteoclast formation. TRAP staining showed many more osteoclasts within *Dmp1^{Cre}:Sox3^{fl/fl}:Csf3r^{-/-}* bone than *Dmp1^{Cre}:Sox3^{fl/fl}* control (Fig. 4A). When quantified, the pore area as a percentage of the cortical area in *Dmp1^{Cre}:Sox3^{fl/fl}:Csf3r^{-/-}* metaphyseal cortical bone was 13.8% greater, and the number of osteoclasts within this area 6.3-fold greater than the already high number of osteoclasts in *Dmp1^{Cre}:Sox3^{fl/fl}* bone (Fig. 4B). Pore size was also significantly

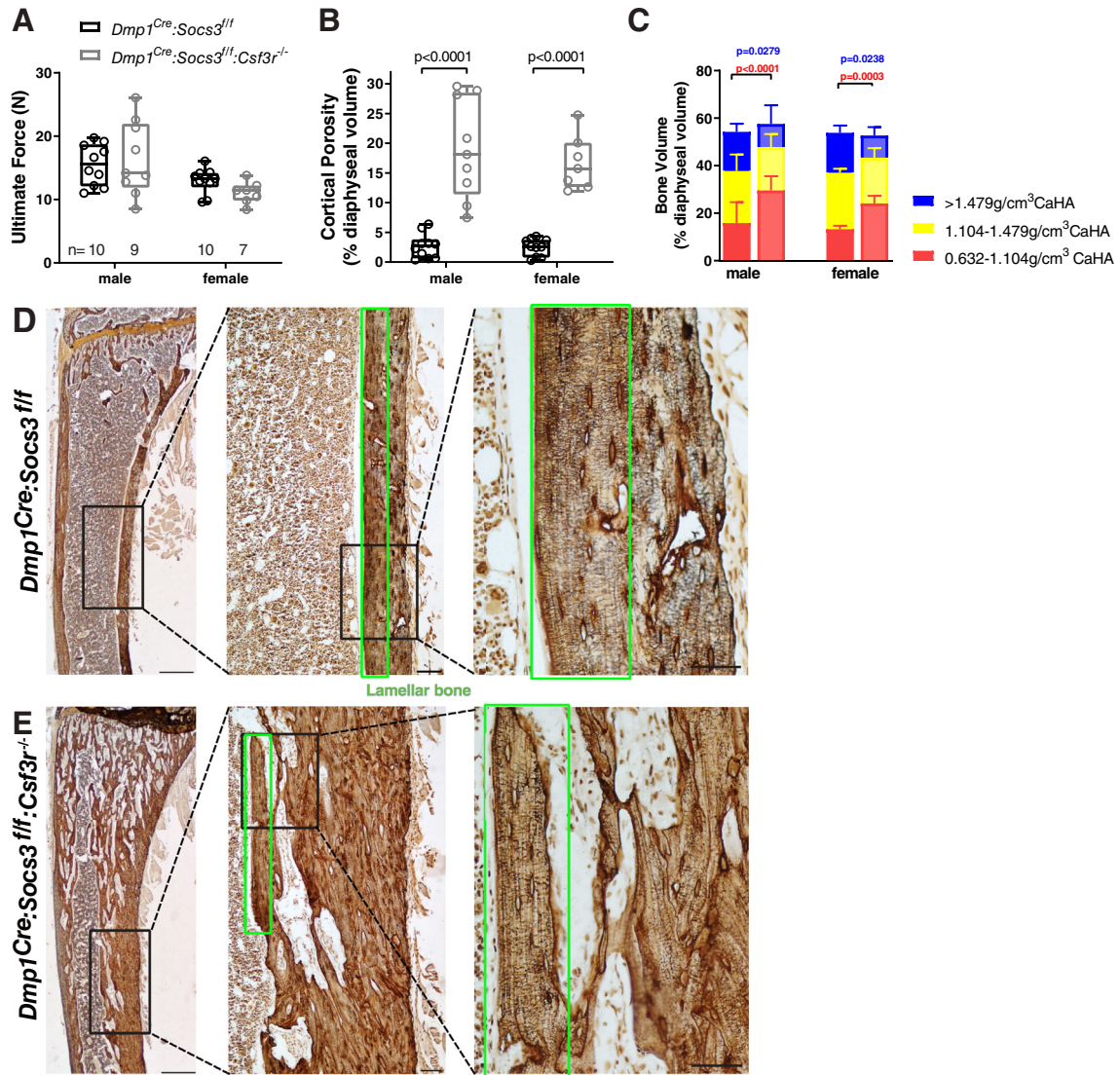


Fig. 3. The delay in cortical maturation in *Dmp1^{Cre}:Socs3^{fl/fl}:Csf3r^{-/-}* mice is associated with greater volume of cortical pores but no change in bone strength. (A) Ultimate force derived from 3-point-bending tests of femora from 12-week-old male and female *Dmp1^{Cre}:Socs3^{fl/fl}* (black circles) and *Dmp1^{Cre}:Socs3^{fl/fl}:Csf3r^{-/-}* (grey circles) mice. Shown are individual values, median, interquartile range, minimum and maximum; *n* reported at base of graph. (B) Femoral diaphyseal cortical porosity at 12 weeks of age of *Dmp1^{Cre}:Socs3^{fl/fl}* and *Dmp1^{Cre}:Socs3^{fl/fl}:Csf3r^{-/-}* mice. Shown are individual values, median, interquartile range, minimum and maximum; *n* shown in A. (C): bone volume as a percentage of total diaphyseal volume at low-, mid-, and high-density thresholds at 12 weeks of age; *p* values determined by two-way ANOVA with Sidak post hoc test; color of *p* values reflects the bone density level tested. (D, E) Ploton silver staining of tibias from 12-week-old *Dmp1^{Cre}:Socs3^{fl/fl}* (D) and *Dmp1^{Cre}:Socs3^{fl/fl}:Csf3r^{-/-}* (E) mice. Scale bar from left to right = 500 μm, 20 μm, 40 μm. Dashed lines show regions enlarged for each subsequent image. Green box indicates region of lamellar bone.

greater in *Dmp1^{Cre}:Socs3^{fl/fl}:Csf3r^{-/-}* bone than *Dmp1^{Cre}:Socs3^{fl/fl}* control (mean μm² ± SEM, *Dmp1^{Cre}:Socs3^{fl/fl}*: 1053 ± 473, *n* = 5 (2 samples had no visible pores in the sections measured), *Dmp1^{Cre}:Socs3^{fl/fl}:Csf3r^{-/-}*: 5227 ± 3189, *n* = 6; *p* = 0.0431).

Analysis by RT-qPCR of flushed femoral bone samples confirmed the elevation in osteoclasts. Cortical bone prepared from *Dmp1^{Cre}:Socs3^{fl/fl}* mice and *Dmp1^{Cre}* controls at 12 weeks of age had significantly greater *Dcstamp* and *Acp5* mRNA levels with *SOCS3* deletion compared with control mice (Supplemental Table S51), and *Dmp1^{Cre}:Socs3^{fl/fl}:Csf3r^{-/-}* cortical bone showed even higher mRNA levels of osteoclast markers (*Dcstamp* and *Acp5*) (Fig. 4C). The increase in osteoclasts was associated with

a significant elevation in RANKL mRNA (*Tnfsf11*) (Fig. 4C). OPG mRNA (*Tnfrsf11b*) was also significantly elevated (Fig. 4C).

In addition to the high number of osteoclasts, calcein labeling, shown in the same region, indicated elevated bone formation in *Dmp1^{Cre}:Socs3^{fl/fl}:Csf3r^{-/-}* bone compared with *Dmp1^{Cre}:Socs3^{fl/fl}* bone (Fig. 4D). Apart from the periosteum, where double calcein labels were observed, most bone formed was non-lamellar (i.e., woven) bone, and the distance between labels could not be quantified by histomorphometry. The increased bone formation, albeit non-lamellar, was supported by higher levels of mRNA for osteoblast markers (*Alpl* and *Col1a1*) (Fig. 4E) compared with *Dmp1^{Cre}:Socs3^{fl/fl}* bone. This indicates increased bone formation

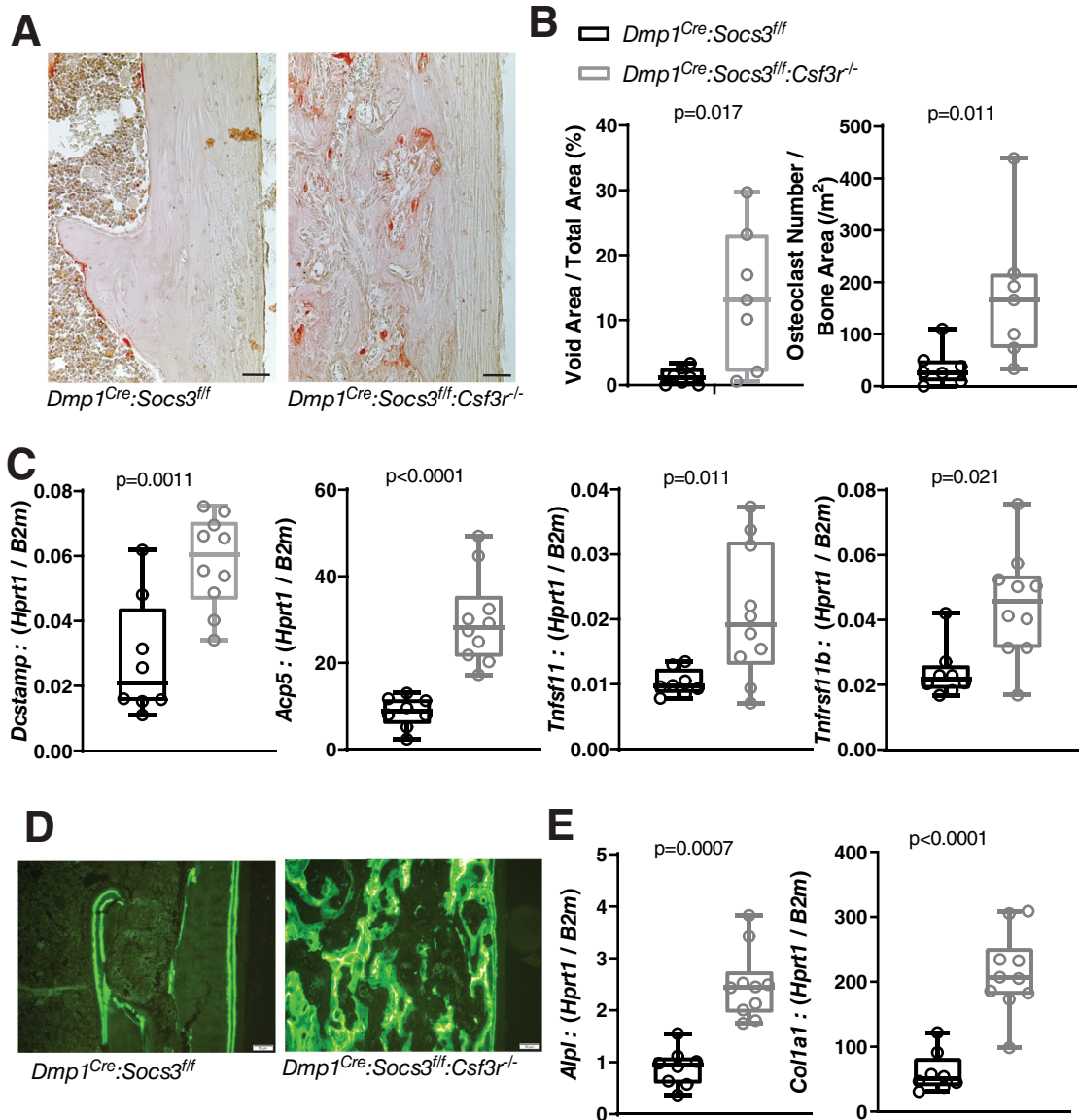


Fig. 4. Increased osteoclasts and bone formation within the cortex of *Dmp1^{Cre}:Socs3^{fl/fl}:Csf3r^{-/-}* bone. (A) Representative images of TRAP staining of tibial lateral metaphyses from 12-week-old *Dmp1^{Cre}:Socs3^{fl/fl}* and *Dmp1^{Cre}:Socs3^{fl/fl}:Csf3r^{-/-}* mice. Scale bar = 50 μ m. (B) Pore area within cortical bone, and osteoclast numbers in the metaphyseal cortical bone of 12-week-old *Dmp1^{Cre}:Socs3^{fl/fl}* and *Dmp1^{Cre}:Socs3^{fl/fl}:Csf3r^{-/-}* mice. Shown are individual values, median, interquartile range, minimum and maximum; (*n* = 7 mice/ group); *p* values determined by Student's *t* test. (C) mRNA levels of osteoclast-related genes *Dcstamp*, *Acp5* (TRAP), *Tnfs11* (RANKL), and *Tnfs11b* (OPG) in flushed femora from 12-week-old *Dmp1^{Cre}:Socs3^{fl/fl}* (*n* = 8) and *Dmp1^{Cre}:Socs3^{fl/fl}:Csf3r^{-/-}* (*n* = 10) mice. Shown are individual values, median, interquartile range, minimum and maximum; *p* values determined by Student's *t* test. (D) Representative images of calcein labeling of tibias from 12-week-old *Dmp1^{Cre}:Socs3^{fl/fl}* (left) and *Dmp1^{Cre}:Socs3^{fl/fl}:Csf3r^{-/-}* (right) mice. Scale bar = 50 μ m. (E) mRNA levels of osteoblast-related genes: *Alpl* (alkaline phosphatase) and *Col1a1* (type I collagen) in flushed femora from 12-week-old *Dmp1^{Cre}:Socs3^{fl/fl}* and *Dmp1^{Cre}:Socs3^{fl/fl}:Csf3r^{-/-}* mice. Shown are individual values, median, interquartile range, minimum and maximum; *n* as in (C); *p* values determined by Student's *t* test.

and resorption in the *Dmp1^{Cre}:Socs3^{fl/fl}:Csf3r^{-/-}* cortex; such a high level of activity is the likely cause of the high level of immature low-density non-lamellar bone in the cortex. This higher level of cortical bone turnover was not associated with any change in serum calcium or phosphate (Table 1).

The extreme delay in cortical bone development in *Dmp1^{Cre}:Socs3^{fl/fl}:Csf3r^{-/-}* mice can therefore be explained by the extremely high levels of osteoblast and osteoclast activity, which

further delays the already prolonged period required for cortical bone consolidation in *Dmp1^{Cre}:Socs3^{fl/fl}* mice.

Increased cortical vascularization is observed in *Dmp1^{Cre}:Socs3^{fl/fl}:Csf3r^{-/-}* bone

Considering the many osteoclasts in *Dmp1^{Cre}:Socs3^{fl/fl}:Csf3r^{-/-}* bone, we sought to determine whether the osteoclast

progenitors were provided by increased vascularization within the cortex. Immunohistochemistry for endomucin revealed greater blood vessel area within the bone cortex, where vessels are usually sparse (Fig. 5A, B). When quantified, there was a 2.9-fold greater blood vessel area in *Dmp1^{Cre}:Socs3^{ff}:Csf3r^{-/-}* bone compared with *Dmp1^{Cre}:Socs3^{ff}* control (Fig. 5C); this increase was due to an increase in vessel number, rather than any change in the size of the blood vessels (Fig. 5D).

RT-qPCR of flushed femora in *Dmp1^{Cre}:Socs3^{ff}:Csf3r^{-/-}* showed two- to fourfold greater mRNA levels of angiogenesis markers (*Emcn*: 3.9-fold, *Tie1*: 2.2-fold, and *Vegfa*: 2.0-fold) (Fig. 5E–G). These parameters were not significantly greater in male *Dmp1^{Cre}:Socs3^{ff}* mice compared with *Dmp1^{Cre}* controls

but were all significantly higher in female *Dmp1^{Cre}:Socs3^{ff}* mice, which had the more severe phenotype in our earlier study (Supplemental Table S51). Deletion of G-CSFR in *Dmp1^{Cre}:Socs3^{ff}* bone therefore increased cortical porosity by increasing both vascularization and osteoclast formation.

FACS analysis of bone marrow confirmed that, consistent with the neutropenia previously observed in *Csf3r^{-/-}* mice,⁽⁴⁶⁾ 12-week-old female *Dmp1^{Cre}:Socs3^{ff}:Csf3r^{-/-}* mice had significantly less neutrophil lineage cells (Gr1⁺CD11b⁺) in bone marrow than sex- and age-matched *Dmp1^{Cre}* and *Dmp1^{Cre}:Socs3^{ff}* mice. Mean neutrophil numbers (% total cells) ± SD: *Dmp1^{Cre}*: 48.78 ± 15.8; *Dmp1^{Cre}:Socs3^{ff}*: 50.61 ± 12.0; *Dmp1^{Cre}:Socs3^{ff}:Csf3r^{-/-}*: 23.4 ± 9.5; *p* = 0.025, one-way ANOVA.

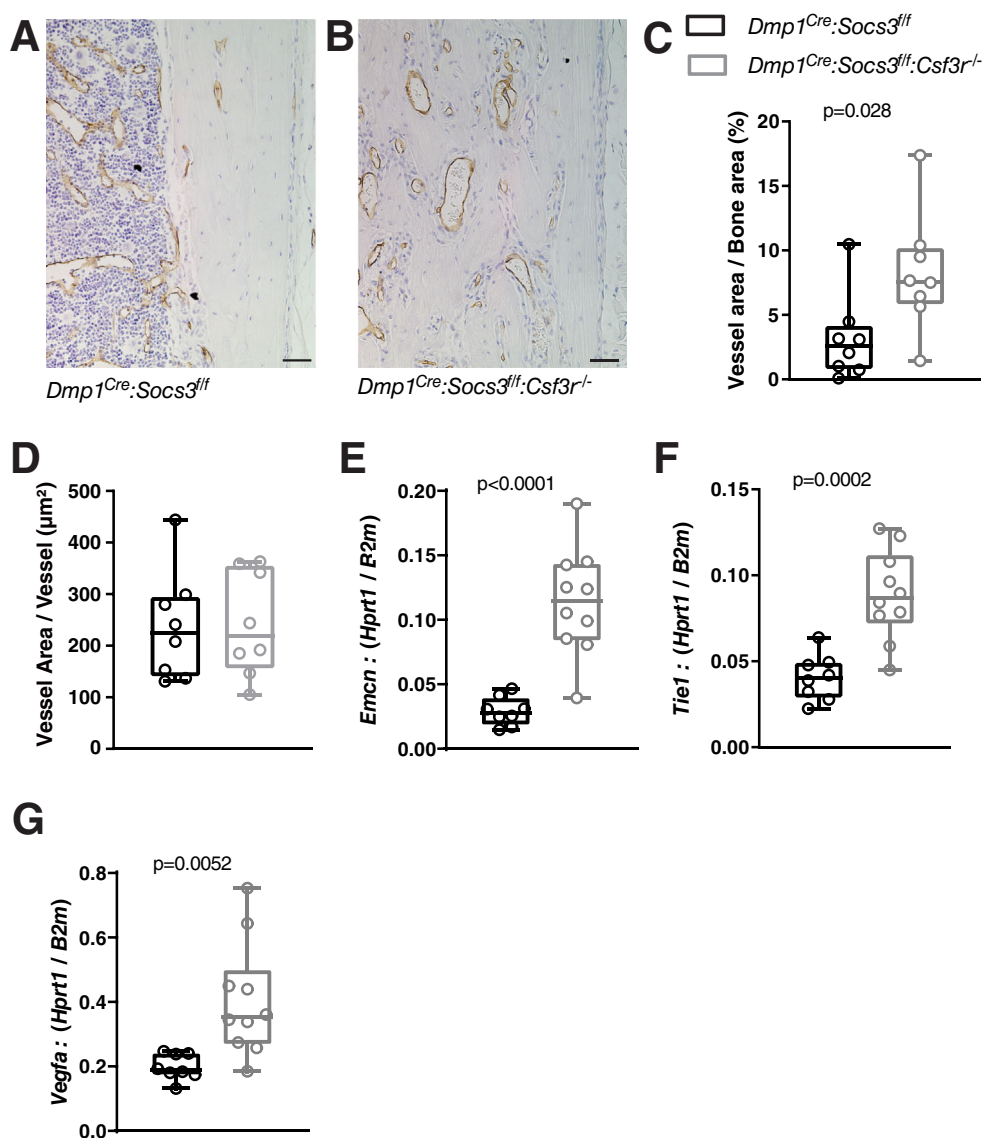


Fig. 5. Increased vascularization within the cortex in *Dmp1^{Cre}:Socs3^{ff}:Csf3r^{-/-}* bone. Endomucin immunohistochemistry images (A, B) and histomorphometry (C, D) of tibial lateral metaphysis from 12-week-old *Dmp1^{Cre}:Socs3^{ff}* (A) and *Dmp1^{Cre}:Socs3^{ff}:Csf3r^{-/-}* (B) tibias. Scale bar = 50 µm. Shown are individual values, median, interquartile range, minimum and maximum; (*n* = 8 mice/ group); *p* values determined by Student's *t* test. (E–G) mRNA levels of vascular genes including Endomucin (*Emcn*), Tie1, and vascular endothelial growth factor A (*Vegfa*) in flushed femora from 12-week-old *Dmp1^{Cre}:Socs3^{ff}* (*n* = 8) and *Dmp1^{Cre}:Socs3^{ff}:Csf3r^{-/-}* (*n* = 10) mice. Shown are individual values, median, interquartile range, minimum and maximum; *p* values determined by Student's *t* test.

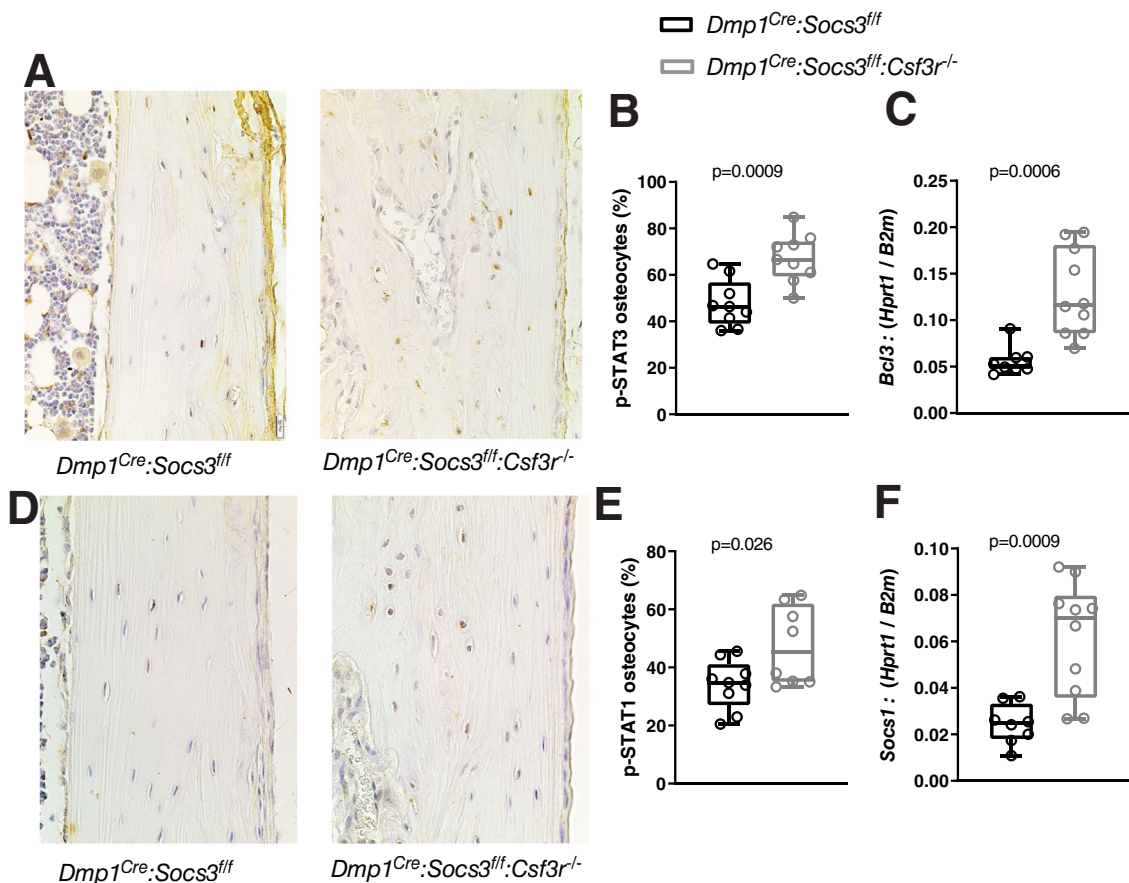


Fig. 6. Granulocyte-colony-stimulating factor receptor (G-CSFR) deletion in *Dmp1^{Cre}.Socs3^{ff}* mice further increases STAT1 and STAT3 signaling in osteocytes. (A, B) Phospho-STAT3 immunohistochemistry and quantitation (B) in osteocytes within the tibial lateral metaphysis from 12-week-old *Dmp1^{Cre}.Socs3^{ff}* and *Dmp1^{Cre}.Socs3^{ff}:Csf3r^{-/-}* mice. Scale bar = 50 μ m. Values are mean \pm SEM ($n = 8-9$ mice/group). The p values determined by Student's t test. (C) mRNA levels of a STAT3 target gene (*Bcl3*) in flushed femora from 12-week-old *Dmp1^{Cre}.Socs3^{ff}* and *Dmp1^{Cre}.Socs3^{ff}:Csf3r^{-/-}* mice. (D, E) Phospho-STAT1 immunohistochemistry and quantitation (E) of tibial lateral metaphysis from 12-week-old *Dmp1^{Cre}.Socs3^{ff}* and *Dmp1^{Cre}.Socs3^{ff}:Csf3r^{-/-}* mice. Scale bar = 50 μ m. (F) mRNA levels of a STAT1 target gene (*Socs1*) in flushed femora from 12-week-old *Dmp1^{Cre}.Socs3^{ff}* and *Dmp1^{Cre}.Socs3^{ff}:Csf3r^{-/-}* mice. All panels show individual values, median, interquartile range, minimum and maximum; ($n = 9$ mice/group). The p values determined by Student's t test.

G-CSFR deletion in *Dmp1^{Cre}.Socs3^{ff}* mice increases STAT1 and STAT3 signaling in osteocytes

To understand the mechanisms leading to increased vascularization, osteoclast formation, and bone formation, and since *Dmp1^{Cre}.Socs3^{ff}* mice exhibited increased STAT3 signaling in osteocytes compared to controls,⁽¹⁰⁾ we next determined whether osteocytic STAT3 signaling was modified by G-CSFR deletion. There was no significant change in total STAT3 staining (mean STAT3-positive osteocytes [% total osteocytes] \pm SD, *Dmp1^{Cre}.Socs3^{ff}*: 31.5% \pm 8.9; *Dmp1^{Cre}.Socs3^{ff}:Csf3r^{-/-}*: 38.5% \pm 11.5, $n = 6$ /group), but the proportion of osteocytes stained positive for phospho-STAT3 phosphorylation was significantly elevated in *Dmp1^{Cre}.Socs3^{ff}:Csf3r^{-/-}* mice compared with *Dmp1^{Cre}.Socs3^{ff}* mice (Fig. 6A, B). This suggests G-CSFR deletion provides additional signals to the osteocyte requiring SOCS3-dependent feedback.

Furthermore, the proportion of osteocytes positive for STAT1 phosphorylation was also elevated (Fig. 6D, E), even though STAT1 phosphorylation was not elevated in *Dmp1^{Cre}.Socs3^{ff}*

mice (Supplemental Fig. SS4). In confirmation of both findings, mRNA levels of STAT3 and STAT1 target genes (*Bcl3* and *Socs1*, respectively) were also elevated in femora from *Dmp1^{Cre}.Socs3^{ff}:Csf3r^{-/-}* mice compared with *Dmp1^{Cre}.Socs3^{ff}* mice (Fig. 6C, F). G-CSFR deletion therefore further increases STAT signaling beyond the already high levels of STAT3 phosphorylation observed in *Dmp1^{Cre}.Socs3^{ff}* mice.

Since G-CSFR has not been detected in cultured osteoblast lineage cells,⁽¹⁸⁾ we tested differentiated OCY454 osteocyte cells and confirmed that they do not express G-CSFR transcript (data not shown). This suggests G-CSFR deficiency in *Dmp1^{Cre}.Socs3^{ff}* mice promotes STAT signaling in osteocytes indirectly.

Discussion

This study shows that global deletion of G-CSFR, although it causes no basal skeletal phenotype, profoundly prolongs the delayed cortical bone consolidation of *Dmp1^{Cre}.Socs3^{ff}* mice.^(5,10) This delay was caused by highly active turnover of the cortex,

characterized by high numbers of osteoclasts, elevated bone formation, and more cortical vascularization than controls, with greater STAT1 and STAT3 phosphorylation in osteocytes of cortical bone.

We previously reported that cortical consolidation requires a lowering of the high levels of bone resorption and formation in very young animals and suggested a threshold of lower activity is necessary for consolidation to occur.⁽⁵⁾ This threshold is reached at a younger age in male mice than females since bone formation and resorption levels decline earlier in males.⁽⁵⁾ This means cortical consolidation in *Dmp1^{Cre}:Socs3^{ff}* mice, while delayed, occurs earlier in male mice⁽⁵⁾ (Fig. 7A). With G-CSFR deletion, still higher levels of both osteoclast formation and bone formation occur in both sexes. This higher level of activity further delays cortical consolidation beyond 12 weeks of age; in male mice, the threshold for consolidation was still not reached by 26 weeks of age, meaning that the cortex was still not fully formed (Fig. 7A). We cannot state whether this is also true for female mice because they died before 26 weeks of age. The high levels of bone resorption and formation are also associated with deposition of woven, rather than lamellar bone, leading to an immature cortical structure, both under normal conditions⁽⁵⁾, and in response to mechanical loading.⁽⁶⁾

This study provides evidence that both bone resorption and bone formation can occur within the pores of murine cortical bone if given sufficient stimulus. Rodent cortical bone, including murine cortical bone, is highly vascularized,^(47,48) and this vascularization normally exhibits an ordered structure with vessels traversing the cortex, recently termed “transcortical vessels.”⁽⁴⁹⁾ Such blood vessels contain both osteoblast⁽⁵⁰⁾ and osteoclast⁽⁴⁹⁾ precursors. Our data suggest STAT3 and possibly STAT1 activation in osteocytes can induce expansion of the transcortical vascular network by angiogenesis. Whether endothelial cells or osteoclasts are first to respond is not known.

SOCS3 provides negative feedback for signaling from multiple cytokines acting through their cognate receptors, including G-CSFR and gp130.⁽⁸⁾ *Dmp1^{Cre}:Socs3^{ff}* bone has a prolonged and augmented STAT3 phosphorylation response to at least three bone-active cytokines signaling through gp130 (IL-11, LIF and OSM).⁽¹⁰⁾ In addition, the high basal STAT3 phosphorylation in *Dmp1^{Cre}:Socs3^{ff}* osteocytes, presumably induced by unsuppressed local action of these cytokines, could be normalized by deleting the gp130 receptor subunit in osteocytes.⁽¹⁰⁾ Here we tested the null hypothesis that unrestrained G-CSFR signaling within osteocytes could also contribute to the *Dmp1^{Cre}:Socs3^{ff}* phenotype using a global null model. We had expected no effect

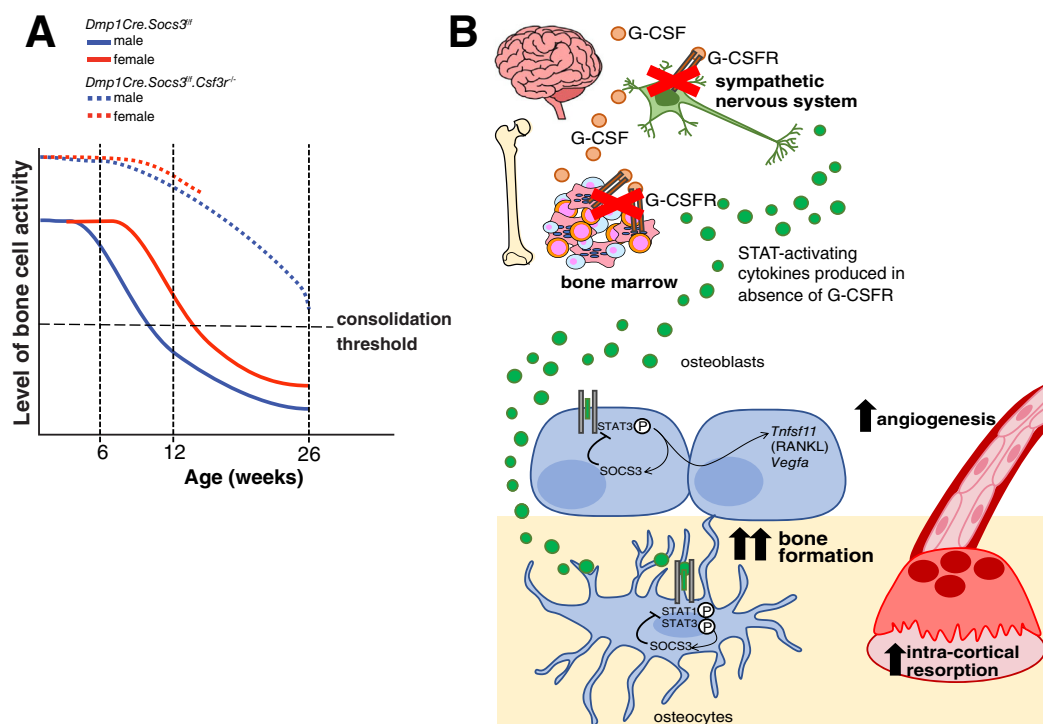


Fig. 7. Two models for the effects of granulocyte-colony-stimulating factor receptor (G-CSF) deletion in bone. (A) A threshold exists at which bone cell activity is sufficiently low for cortical consolidation to occur. In *Dmp1^{Cre}:Socs3^{ff}* mice, bone cell activity gradually reduces with age, with male mice reaching the threshold for consolidation before females. With deletion of G-CSFR in *Dmp1^{Cre}:Socs3^{ff}:Csf3r^{-/-}* mice, there are still higher levels of bone resorption and bone formation, such that both male and female mice are above the threshold for cortical consolidation even at 26 weeks of age. (B) G-CSF acts on cells of the sympathetic nervous system and the bone marrow, including neutrophils and macrophages. In the absence of G-CSFR, one or more of these cell types produce a signal that, either directly or indirectly, stimulates STAT3 phosphorylation in osteoblasts and osteocytes. This signal is normally suppressed by SOCS3. However, when STAT1 and STAT3 signaling cannot be suppressed in these cells (eg, by genetic deletion of SOCS3 in *Dmp1^{Cre}:Socs3^{ff}* mice), increased signaling stimulates osteoblast differentiation and bone formation. It also increases *Tnfsf11* (RANKL) and *Vegfa* expression within bone, leading to more angiogenesis within the cortical bone and more cortical bone resorption by osteoclasts. This latter effect prevents formation of a consolidated cortex.

of G-CSFR deletion because G-CSFR is not expressed in osteocytes and because no bone phenotype was observed in G-CSFR null mice. However, we were surprised to observe a profound bone phenotype, revealing that G-CSF inhibits cortical bone resorption, bone formation, and vascularization in the context of elevated STAT3 signaling in bone.

Since no effect of G-CSF deletion alone was observed on the skeleton, this new role of G-CSF as an inhibitor of bone formation and resorption is required only in conditions when osteocytic STAT3 signaling is elevated. This could include states previously reported to increase STAT3 signalling such as inflammation or mechanical loading.^(6,51) Indeed, we have recently observed formation of more porous and woven bone in *Dmp1Cre.Socs3^{fl/fl}* tibias than control tibias subjected to the same mechanical load.⁽⁶⁾ It is also possible that elevated STAT3 signaling is a property of woven bone, and the high level of STAT3 signaling observed in G-CSFR deficiency when SOCS3 is removed is a result, rather than a cause of the phenotype, but this is a speculation only.

The lack of any discernible basal phenotype in G-CSFR deficiency implies that SOCS3 negative feedback in osteocytes is normally sufficient to enable skeletal maturation in the absence of G-CSFR even if the G-CSFR null mice produce signals that induce STAT1 and STAT3 phosphorylation in osteocytes. However, when the STAT3 and STAT1 responses are not suppressed by SOCS3 due to genetic deletion, they are then sufficient to induce pro-vascularization and pro-osteoclast factors, such as VEGFA and RANKL. This, at least in the case of RANKL, is an exaggeration of the known effect of STAT3 signaling in osteoblast lineage cells to initiate osteoclast formation via RANKL production in response to a range of hormones and cytokines.^(16,52) Bone marrow cells reported to express the G-CSFR, such as macrophages⁽⁵³⁾ and neutrophils,⁽⁵⁴⁾ produce multiple cytokines that activate STAT3 in osteoblasts and stimulate both their differentiation and their production of RANKL (reviewed in⁽⁵⁵⁾). Most notable is OSM, which is a mediator by which macrophages promote bone formation;⁽⁵⁶⁻⁵⁹⁾ other macrophage- and neutrophil-derived STAT3-dependent cytokines, such as IL-6, could have a similar role. Sympathetic neurons also express G-CSFR⁽⁶⁰⁾ and produce STAT3-dependent cytokines such as ciliary neurotrophic factor, LIF, cardiotrophin 1, and IL-6.⁽⁶¹⁻⁶³⁾ These, too, regulate osteoblast differentiation and production of RANKL by the osteoblast lineage.^(12,15,64,65) Whether these cytokines influence skeletal structure through the sympathetic nervous system is not known, but other factors, including leptin, regulate both bone formation and resorption through this pathway,^(66,67) suggesting this possibility. Much further work would be required to identify the elevated cytokines responsible, and the cells producing them, using a combination of proteomics and single-cell RNA-sequencing; ultimate proof of causation will require targeted genetic knockdown of the candidate cytokines.

The only known phenotype of G-CSFR null mice under basal conditions is a profound neutropenia, including very low levels of marrow-residing immature neutrophils (metamyelocytes, band neutrophils, and segmented neutrophils).⁽⁴⁶⁾ We also detected low levels of marrow neutrophil populations in the *Dmp1Cre.Socs3^{fl/fl}.Csf3r^{-/-}* mice. This may contribute to the bone phenotype of these mice, although there is no current data linking neutrophil progenitors in the marrow to bone structure. This would contrast with the effect of mature, circulating neutrophils on bone, which have been studied only in pathological conditions such as rheumatoid arthritis and periodontitis, where neutrophils express RANKL^(68,69) and neutrophil depletion reduces focal bone erosion^(69,70) by reducing local inflammation.⁽⁷¹⁾

Despite the greater diaphyseal cortical porosity in *Dmp1^{Cre}.Socs3^{fl/fl}.Csf3r^{-/-}* femurs, three-point bending test markers of bone strength were not weakened compared with *Dmp1^{Cre}.Socs3^{fl/fl}* controls. The distinct cortical bone structure in *Dmp1^{Cre}.Socs3^{fl/fl}.Csf3r^{-/-}* mice includes regions of normal lamellar bone alongside a channel of highly porous woven bone; together, this thickened, albeit porous, cortex clearly provides sufficient strength. A similar “double shell” of bone with a porous channel in the primordial cortex occurs when the cortex emerges during the prenatal and early postnatal period,⁽⁷²⁾ suggesting deposition of lamellar cortical bone on an internal porous structure could be a compensatory mechanism to maintain cortical strength.

To summarize (Fig. 7B), G-CSFR deletion on its own has no impact on bone structure, but in mice lacking SOCS3 in osteocytes, G-CSFR deletion promotes STAT1 and STAT3 phosphorylation in osteocytes, leading to increased cortical angiogenesis and bone resorption, ultimately leading to elevated remodeling of cortical bone through to adulthood. We conclude that G-CSFR signaling could indirectly limit bone resorption and angiogenesis and thereby has a critical role in replacing the condensed trabecular bone with lamellar bone during cortical bone structural consolidation.

Disclosures

All authors state that they have no conflicts of interest.

Acknowledgments

The authors thank the staff of the St. Vincent's Health Melbourne BioResources Centre for excellent animal care, Blessing Crimeen-Irwin for flow cytometry analysis, and Prof J P Levesque for helpful discussions of the work.

This work was funded by an NHMRC (Australia) project grant (1120978) and Senior Research Fellowship (1154819) to NAS, and philanthropic support to St. Vincent's Institute. TI was supported by travel grants from Mochida Memorial Foundation for Medical and Pharmacological Research and The Foundation for Growth Science, Japan. St. Vincent's Institute also receives Operational Infrastructure Support from the Victorian State Government.

Authors' roles: TI: formal analysis, investigation, methodology, writing—original draft, and writing—review & editing. ECW: formal analysis, investigation, methodology, visualization, and writing—review & editing. IJP: formal analysis, investigation, methodology, and writing—review & editing. NEM: formal analysis, investigation, methodology, and writing—review & editing. IPW: resources and writing—review & editing. JHG: formal analysis, investigation, methodology, and writing—review & editing. TJM: conceptualization, investigation, and writing—review & editing. NAS: conceptualization, data curation, formal analysis, funding acquisition, investigation, methodology, project administration, supervision, visualization, and writing—review & editing.

Author Contributions

Tsuyoshi Isojima: Formal analysis; investigation; methodology; writing – original draft; writing – review and editing. **Emma C Walker:** Formal analysis; investigation; methodology; visualization; writing – review and editing. **Ingrid J Poulton:** Formal

analysis; investigation; methodology; writing – review and editing. **Narelle E McGregor:** Formal analysis; investigation; methodology; writing – review and editing. **Ian P Wicks:** Resources; writing – review and editing. **Jonathan H Gooi:** Formal analysis; investigation; methodology; writing – review and editing. **T John Martin:** Conceptualization; investigation; writing – review and editing. **Natalie A Sims:** Conceptualization; data curation; formal analysis; funding acquisition; investigation; methodology; project administration; supervision; visualization; writing – review and editing.

Peer Review

The peer review history for this article is available at <https://publons.com/publon/10.1002/jbmr.4654>.

Data Availability Statement

Data available on request from the authors

References

1. Enlow DH. A study of the post-natal growth and remodeling of bone. *Am J Anat.* 1962;110:79-101.
2. Rauch F. The dynamics of bone structure development during pubertal growth. *J Musculoskelet Neuronal Interact.* 2012;12(1):1-6.
3. Maggiano IS, Maggiano CM, Tiesler VG, Chi-Keb JR, Stout SD. Drifting diaphyses: asymmetry in diametric growth and adaptation along the humeral and femoral length. *Anat Rec.* 2015;298(10):1689-1699.
4. Isojima T, Sims NA. Cortical bone development, maintenance and porosity: genetic alterations in humans and mice influencing chondrocytes, osteoclasts, osteoblasts and osteocytes. *Cell Mol Life Sci.* 2021;78(15):5755-5773.
5. Cho DC, Brennan HJ, Johnson RW, et al. Bone corticalization requires local SOCS3 activity and is promoted by androgen action via interleukin-6. *Nat Commun.* 2017;8(1):806.
6. McGregor NE, Walker EC, Chan AS, et al. STAT3 hyperactivation due to SOCS3 deletion in murine osteocytes accentuates responses to exercise- and load-induced bone formation. *J Bone Miner Res.* 2022;37(3):547-558.
7. Liu X, D'Cruz AA, Hansen J, et al. Deleting suppressor of cytokine signaling-3 in chondrocytes reduces bone growth by disrupting mitogen-activated protein kinase signaling. *Osteoarthritis Cartilage.* 2019;27(10):1557-1563.
8. Morris R, Kershaw NJ, Babon JJ. The molecular details of cytokine signaling via the JAK/STAT pathway. *Protein Sci.* 2018;27(12):1984-2009.
9. Babon JJ, Nicola NA. The biology and mechanism of action of suppressor of cytokine signaling 3. *Growth Factors.* 2012;30(4):207-219.
10. Walker EC, Truong K, McGregor NE, et al. Cortical bone maturation in mice requires SOCS3 suppression of gp130/STAT3 signalling in osteocytes. *Elife.* 2020;9:e56666.
11. Sims NA, Jenkins BJ, Nakamura A, et al. Interleukin-11 receptor signaling is required for normal bone remodeling. *J Bone Miner Res.* 2005;20(7):1093-1102.
12. Poulton IJ, McGregor NE, Pompolo S, Walker EC, Sims NA. Contrasting roles of leukemia inhibitory factor in murine bone development and remodeling involve region-specific changes in vascularization. *J Bone Miner Res.* 2012;27(3):586-595.
13. Song HY, Jeon ES, Kim JI, Jung JS, Kim JH. Oncostatin M promotes osteogenesis and suppresses adipogenic differentiation of human adipose tissue-derived mesenchymal stem cells. *J Cell Biochem.* 2007;101(5):1238-1251.
14. Tamura T, Udagawa N, Takahashi N, et al. Soluble interleukin-6 receptor triggers osteoclast formation by interleukin 6. *Proc Natl Acad Sci U S A.* 1993;90(24):11924-11928.
15. Walker EC, McGregor NE, Poulton IJ, et al. Cardiotrophin-1 is an osteoclast-derived stimulus of bone formation required for normal bone remodeling. *J Bone Miner Res.* 2008;23(12):2025-2032.
16. Sims NA. The JAK1/STAT3/SOCS3 axis in bone development, physiology, and pathology. *Exp Mol Med.* 2020;52(8):1185-1197.
17. Semerad CL, Christopher MJ, Liu F, et al. G-CSF potently inhibits osteoblast activity and CXCL12 mRNA expression in the bone marrow. *Blood.* 2005;106(9):3020-3027.
18. Katayama Y, Battista M, Kao WM, et al. Signals from the sympathetic nervous system regulate hematopoietic stem cell egress from bone marrow. *Cell.* 2006;124(2):407-421.
19. Winkler IG, Sims NA, Pettit AR, et al. Bone marrow macrophages maintain hematopoietic stem cell (HSC) niches and their depletion mobilizes HSCs. *Blood.* 2010;116(23):4815-4828.
20. Winkler IG, Pettit AR, Raggatt LJ, et al. Hematopoietic stem cell mobilizing agents G-CSF, cyclophosphamide or AMD3100 have distinct mechanisms of action on bone marrow HSC niches and bone formation. *Leukemia.* 2012;26(7):1594-1601.
21. Asada N, Katayama Y, Sato M, et al. Matrix-embedded osteocytes regulate mobilization of hematopoietic stem/progenitor cells. *Cell Stem Cell.* 2013;12(6):737-747.
22. Takamatsu Y, Simmons PJ, Moore RJ, Morris HA, To LB, Levesque JP. Osteoclast-mediated bone resorption is stimulated during short-term administration of granulocyte colony-stimulating factor but is not responsible for hematopoietic progenitor cell mobilization. *Blood.* 1998;92(9):3465-3473.
23. Lu Y, Xie Y, Zhang S, Dusevich V, Bonewald LF, Feng JQ. DMP1-targeted Cre expression in odontoblasts and osteocytes. *J Dent Res.* 2007;86(4):320-325.
24. Croker BA, Krebs DL, Zhang JG, et al. SOCS3 negatively regulates IL-6 signaling in vivo. *Nat Immunol.* 2003;4(6):540-545.
25. Walker EC, Johnson RW, Hu Y, et al. Murine oncostatin M acts via leukemia inhibitory factor receptor to phosphorylate signal transducer and activator of transcription 3 (STAT3) but not STAT1, an effect that protects bone mass. *J Biol Chem.* 2016;291(41):21703-21716.
26. Ansari N, Ho PW, Crimeen-Irwin B, et al. Autocrine and paracrine regulation of the murine skeleton by osteocyte-derived parathyroid hormone-related protein. *J Bone Miner Res.* 2018;33(1):137-153.
27. Ansari N, Isojima T, Crimeen-Irwin B, et al. Dmp1Cre-directed knock-down of parathyroid hormone-related protein (PTHrP) in murine decidua is associated with a life-long increase in bone mass, width, and strength in male progeny. *J Bone Miner Res.* 2021;36(10):1999-2016.
28. Walker EC, McGregor NE, Chan ASM, Sims NA. Measuring bone volume at multiple densities by micro-computed tomography. *Bio Protoc.* 2021;11(1):e3873.
29. Otsu N. A threshold selection method from gray-level histograms. *IEEE Trans Syst Man Cybern.* 1979;9(1):62-66.
30. Sims NA, Clement-Lacroix P, Da Ponte F, et al. Bone homeostasis in growth hormone receptor-null mice is restored by IGF-1 but independent of Stat5. *J Clin Invest.* 2000;106(9):1095-1103.
31. Sims NA, White CP, Sunn KL, et al. Human and murine osteocalcin gene expression: conserved tissue restricted expression and divergent responses to 1, 25-dihydroxyvitamin D3 in vivo. *Mol Endocrinol.* 1997;11(11):1695-1708.
32. Jauregui EJ, Akil O, Acevedo C, et al. Parallel mechanisms suppress cochlear bone remodeling to protect hearing. *Bone.* 2016;89:7-15.
33. Sims NA, Jenkins BJ, Quinn JM, et al. Glycoprotein 130 regulates bone turnover and bone size by distinct downstream signaling pathways. *J Clin Invest.* 2004;113(3):379-389.
34. Williamson L, Hayes A, Hanson ED, Pivonka P, Sims NA, Gooi JH. High dose dietary vitamin D3 increases bone mass and strength in mice. *Bone Rep.* 2017;6:44-50.
35. Jepsen KJ, Silva MJ, Vashishth D, Guo XE, van der Meulen MC. Establishing biomechanical mechanisms in mouse models: practical guidelines for systematically evaluating phenotypic changes in the diaphyses of long bones. *J Bone Miner Res.* 2015;30(6):951-966.
36. Walker EC, Poulton IJ, McGregor NE, et al. Sustained RANKL response to parathyroid hormone in oncostatin M receptor-deficient

- osteoblasts converts anabolic treatment to a catabolic effect in vivo. *J Bone Miner Res.* 2012;27(4):902-912.
37. McGregor NE, Murat M, Elango J, et al. IL-6 exhibits both cis- and trans-signaling in osteocytes and osteoblasts, but only trans-signaling promotes bone formation and osteoclastogenesis. *J Biol Chem.* 2019;294(19):7850-7863.
 38. Onan D, Allan EH, Quinn JM, et al. The chemokine Cxcl1 is a novel target gene of parathyroid hormone (PTH)/PTH-related protein in committed osteoblasts. *Endocrinology.* 2009;150(5):2244-2253.
 39. Takyar FM, Tonna S, Ho PW, et al. EphrinB2/EphB4 inhibition in the osteoblast lineage modifies the anabolic response to parathyroid hormone. *J Bone Miner Res.* 2013;28(4):912-925.
 40. Allan EH, Hausler KD, Wei T, et al. EphrinB2 regulation by PTH and PTHrP revealed by molecular profiling in differentiating osteoblasts. *J Bone Miner Res.* 2008;23(8):1170-1181.
 41. Nakamura A, Ly C, Cipetic M, et al. Osteoclast inhibitory lectin (OCIL) inhibits osteoblast differentiation and function in vitro. *Bone.* 2007;40(2):305-315.
 42. Gooi JH, Pompolo S, Karsdal MA, et al. Calcitonin impairs the anabolic effect of PTH in young rats and stimulates expression of sclerostin by osteocytes. *Bone.* 2010;46(6):1486-1497.
 43. Winkler IG, Hendy J, Coughlin P, Horvath A, Lévesque JP. Serine protease inhibitors serpin1 and serpin3 are down-regulated in bone marrow during hematopoietic progenitor mobilization. *J Exp Med.* 2005;201(7):1077-1088.
 44. Buie HR, Campbell GM, Klinck RJ, MacNeil JA, Boyd SK. Automatic segmentation of cortical and trabecular compartments based on a dual threshold technique for in vivo micro-CT bone analysis. *Bone.* 2007;41(4):505-515.
 45. Bouxsein ML, Boyd SK, Christiansen BA, Guldberg RE, Jepsen KJ, Müller R. Guidelines for assessment of bone microstructure in rodents using micro-computed tomography. *J Bone Miner Res.* 2010;25(7):1468-1486.
 46. Liu F, Wu HY, Wesselschmidt R, Kornaga T, Link DC. Impaired production and increased apoptosis of neutrophils in granulocyte colony-stimulating factor receptor-deficient mice. *Immunity.* 1996;5(5):491-501.
 47. De Saint-Georges L, Miller SC. The microcirculation of bone and marrow in the diaphysis of the rat hemopoietic long bones. *Anat Rec.* 1992;233(2):169-177.
 48. Asghar A, Kumar A, Kant Narayan R, Naaz S. Is the cortical capillary renamed as the transcortical vessel in diaphyseal vascularity? *Anat Rec.* 2020;303(11):2774-2784.
 49. Grüneboom A, Hawwari I, Weidner D, et al. A network of trans-cortical capillaries as mainstay for blood circulation in long bones. *Nat Metab.* 2019;1(2):236-250.
 50. Root SH, Wee NKY, Novak S, et al. Perivascular osteoprogenitors are associated with transcortical channels of long bones. *Stem Cells.* 2020;38(6):769-781.
 51. Corry KA, Zhou H, Brustovetsky T, et al. Stat3 in osteocytes mediates osteogenic response to loading. *Bone Rep.* 2019;11:100218.
 52. O'Brien CA, Gubrij I, Lin SC, Saylor RL, Manolagas SC. STAT3 activation in stromal/osteoblastic cells is required for induction of the receptor activator of NF-kappaB ligand and stimulation of osteoclastogenesis by gp130-utilizing cytokines or interleukin-1 but not 1,25-dihydroxyvitamin D3 or parathyroid hormone. *J Biol Chem.* 1999;274(27):19301-19308.
 53. Christopher MJ, Rao M, Liu F, Woloszynek JR, Link DC. Expression of the G-CSF receptor in monocytic cells is sufficient to mediate hematopoietic progenitor mobilization by G-CSF in mice. *J Exp Med.* 2011;208(2):251-260.
 54. Nicola NA, Metcalf D. Binding of 125I-labeled granulocyte colony-stimulating factor to normal murine hemopoietic cells. *J Cell Physiol.* 1985;124(2):313-321.
 55. Sims NA. Influences of the IL-6 cytokine family on bone structure and function. *Cytokine.* 2021;146:155655.
 56. Fernandes TJ, Hodge JM, Singh PP, et al. Cord blood-derived macrophage-lineage cells rapidly stimulate osteoblastic maturation in mesenchymal stem cells in a glycoprotein-130 dependent manner. *PLoS One.* 2013;8(9):e73266.
 57. Nicolaidou V, Wong MM, Redpath AN, et al. Monocytes induce STAT3 activation in human mesenchymal stem cells to promote osteoblast formation. *PLoS One.* 2012;7(7):e39871.
 58. Torossian F, Guerton B, Anginot A, et al. Macrophage-derived oncostatin M contributes to human and mouse neurogenic heterotopic ossifications. *JCI Insight.* 2017;2(21):396034.
 59. Guihard P, Boutet MA, Brounais-Le Royer B, et al. Oncostatin M, an inflammatory cytokine produced by macrophages, supports intramembranous bone healing in a mouse model of tibia injury. *Am J Pathol.* 2015;185(3):765-775.
 60. Schweizerhof M, Stösser S, Kurejova M, et al. Hematopoietic colony-stimulating factors mediate tumor-nerve interactions and bone cancer pain. *Nat Med.* 2009;15(7):802-807.
 61. Ludlam WH, Kessler JA. Leukemia inhibitory factor and ciliary neurotrophic factor regulate expression of muscarinic receptors in cultured sympathetic neurons. *Dev Biol.* 1993;155(2):497-506.
 62. Cheng J-G, Pennica D, Patterson PH. Cardiostrophin-1 induces the same neuropeptides in sympathetic neurons as do neurotrophic cytokines. *J Neurochem.* 1997;69(6):2278-2284.
 63. März P, Cheng J-G, Gadiant RA, et al. Sympathetic neurons can produce and respond to interleukin 6. *Proc Natl Acad Sci.* 1998;95(6):3251-3256.
 64. McGregor NE, Poulton IJ, Walker EC, et al. Ciliary neurotrophic factor inhibits bone formation and plays a sex-specific role in bone growth and remodeling. *Calcif Tissue Int.* 2010;86(3):261-270.
 65. Palmqvist P, Persson E, Conaway HH, Lerner UH. IL-6, leukemia inhibitory factor, and oncostatin M stimulate bone resorption and regulate the expression of receptor activator of NF-kappa B ligand, osteoprotegerin, and receptor activator of NF-kappa B in mouse calvariae. *J Immunol.* 2002;169(6):3353-3362.
 66. Takeda S, Eleftheriou F, Lévassieur R, et al. Leptin regulates bone formation via the sympathetic nervous system. *Cell.* 2002;111(3):305-317.
 67. Eleftheriou F, Ahn JD, Takeda S, et al. Leptin regulation of bone resorption by the sympathetic nervous system and CART. *Nature.* 2005;434(7032):514-520.
 68. Poubelle PE, Chakravarti A, Fernandes MJ, Doiron K, Marceau A-A. Differential expression of RANK, RANK-L, and osteoprotegerin by synovial fluid neutrophils from patients with rheumatoid arthritis and by healthy human blood neutrophils. *Arthritis Res Ther.* 2007;9(2):R25.
 69. Kim AR, Kim JH, Choi YH, et al. The presence of neutrophils causes RANKL expression in periodontal tissue, giving rise to osteoclast formation. *J Periodontol Res.* 2020;55(6):868-876.
 70. Lee MC, McCubbin JA, Christensen AD, et al. G-CSF receptor blockade ameliorates arthritic pain and disease. *J Immunol.* 2017;198(9):3565-3575.
 71. Eyles JL, Hickey MJ, Norman MU, et al. A key role for G-CSF-induced neutrophil production and trafficking during inflammatory arthritis. *Blood.* 2008;112(13):5193-5201.
 72. Sharir A, Stern T, Rot C, Shahar R, Zelzer E. Muscle force regulates bone shaping for optimal load-bearing capacity during embryogenesis. *Development.* 2011;138(15):3247-3259.
 73. Ling YC, Nicole C, Walsh, T. John M, Natalie A. Sims, Isolation and gene expression of haematopoietic-cell-free preparations of highly purified murine osteocytes. *Bone.* 2015;72:34-42.